

**THE MILLIMETER-WAVELENGTH SULFUR DIOXIDE
ABSORPTION SPECTRA MEASURED UNDER
SIMULATED VENUS CONDITIONS**

A Thesis
Presented to
The Academic Faculty

by

Amadeo Bellotti

In Partial Fulfillment
of the Requirements for the Degree
Master of Science in the
School of Electrical and Computer Engineering

Georgia Institute of Technology
May 2015

**THE MILLIMETER-WAVELENGTH SULFUR DIOXIDE
ABSORPTION SPECTRA MEASURED UNDER
SIMULATED VENUS CONDITIONS**

Approved by:

Professor Paul G. Steffes, Advisor
School of Electrical and Computer
Engineering
Georgia Institute of Technology

Professor Morris B. Cohen
School of Electrical and Computer
Engineering
Georgia Institute of Technology

Professor Andrew F. Peterson
School of Electrical and Computer
Engineering
Georgia Institute of Technology

Date Approved: TBD

To my parents,

Who are always putting education first.

ACKNOWLEDGEMENTS

I would like to express my deepest gratitude to my adviser Professor Paul Steffes for his support and guidance throughout the course of this research. His constant wealth of knowledge, support, and patience helped me in completing this work. Although electromagnetism, and planetary remote sensing are not fields I would have seen myself working with during my undergraduate years, Dr. Steffes, eased me into it in a way I feel allowed me to grow and enjoy it. I would also like to thank my committee members Dr. Morris B. Cohen and Dr. Andrew F. Peterson for providing me with the time and effort in carefully reviewing my thesis work.

The success of the laboratory experiments was made possible as a result of many contributions. I wish to thank Dr. Kirtuthika Devaraj for creating and automating the millimeter-wavelength measurement system and Dr. Thomas Hanley for providing the data processing code. Both of these were utilized in this research work.

The constant support and encouragement from my family has allowed me to pursue my goals throughout these years. I cannot thank them enough for pushing me to go to graduate school.

TABLE OF CONTENTS

DEDICATION	iii
ACKNOWLEDGEMENTS	iv
LIST OF TABLES	vii
LIST OF FIGURES	viii
I INTRODUCTION	1
1.1 Background and Motivation	2
1.2 Organization	3
II EXPERIMENT DESIGN, THEORY, AND RESULTS	5
2.1 Measurement Theory	5
2.2 Millimeter-Wavelength Measurement System	7
2.2.1 W-band Subsystem	7
2.2.2 F-band Subsystem	9
2.3 Data Handling Subsystem	10
2.4 Measurement Procedure	11
III MODEL FITTING AND MODIFICATIONS	13
3.1 Measurement Uncertainties	13
3.2 Model Analysis Process	20
3.3 Experimental Results	22
3.3.1 Accuracy of Constituents	22
3.4 Suggested Model	32
IV RADIATIVE TRANSFER MODEL OF THE VENUS ATMOSPHERE	33
4.1 Theoretical Background	33
4.2 Parameters of the Radiative Transfer Model	36
4.2.1 Temperature-Pressure Profiles	37
4.2.2 Opacity Formalisms	37

4.2.3	Abundance Profiles	41
4.2.4	Index of Refraction	42
4.3	Ray-tracing	42
4.3.1	Ray-tracing Described	42
4.3.2	Ray-tracing Algorithm Mathematics	45
4.4	Vector Radiative Transfer	49
4.4.1	Thermo-Chemical Model (TCM)	49
4.4.2	Absorption Matrix	49
4.4.3	Ray-Tracing	50
4.4.4	Radiative Transfer Model	50
4.5	Beam Forming	51
4.6	Radiative Transfer Results	52
V	SUMMARY AND CONCLUSIONS	55
5.1	Significant Results	55
5.2	Application to Venus Observations	56
5.3	Suggestions for Future Work	57
	APPENDIX A — REFRACTIVITY OF SO₂	58
	REFERENCES	63

LIST OF TABLES

1	The percentage of the measured data points within 2σ uncertainty of the different models	21
2	Measured Disk-Averaged Brightness Temperatures of Venus for Various Frequencies as compared to the results from the new Radiative Transfer Model	53
3	Normalized refractivity of SO ₂ in a CO ₂ atmosphere.	58

LIST OF FIGURES

2.1	Block diagram of the W-band measurement system. Solid lines represent the electrical connections and the arrows show the direction of the signal propagation. Valves controlling the flow of gasses are shown by small crossed circles.	8
2.2	Block diagram of the F-band measurement system. Solid lines represent the electrical connections and the arrows show the direction of the signal propagation. Valves controlling the flow of gasses are shown by small crossed circles.	10
3.1	Opacity data using the 2-3 mm-wavelength system for a mixture of $\text{SO}_2 = 84.7\%$, $\text{CO}_2 = 0\%$ at a pressure of 0.030 bar and a temperature of 308.8 K compared to various models	23
3.2	Opacity data using the 2-3 mm-wavelength system for a mixture of $\text{SO}_2 = 2.6\%$, $\text{CO}_2 = 96.9\%$ at a pressure of 0.970 bar and a temperature of 308.5 K compared to various models	23
3.3	Opacity data using the 2-3 mm-wavelength system for a mixture of $\text{SO}_2 = 1.3\%$, $\text{CO}_2 = 98.5\%$ at a pressure of 1.995 bar and a temperature of 308.6 K compared to various models	24
3.4	Opacity data using the 3-4 mm-wavelength system for a mixture of $\text{SO}_2 = 84.7\%$, $\text{CO}_2 = 0\%$ at a pressure of 0.116 bar and a temperature of 307.5 K compared to various models	24
3.5	Opacity data using the 2.7-4 mm-wavelength system for a mixture of $\text{SO}_2 = 10.4\%$, $\text{CO}_2 = 87.7\%$ at a pressure of 0.943 bar and a temperature of 307.2 K compared to various models	25
3.6	Opacity data using the 2.7-4 mm-wavelength system for a mixture of $\text{SO}_2 = 4.9\%$ and $\text{CO}_2 = 94.2\%$ at a pressure of 1.987 bar and a temperature of 307.2 K compared to various models	25
3.7	Opacity data using the 2-3 mm-wavelength system for a mixture of $\text{SO}_2 = 84.7\%$ and $\text{CO}_2 = 0\%$ at a pressure of 0.090 bar and a temperature of 344.4 K compared to various models	26
3.8	Opacity data using the 2-3 mm-wavelength system for a mixture of $\text{SO}_2 = 8.3\%$ and $\text{CO}_2 = 90.2\%$ at a pressure of 0.923 bar and a temperature of 344.6 K compared to various models	26
3.9	Opacity data using the 2-3 mm-wavelength system for a mixture of $\text{SO}_2 = 3.9\%$ and $\text{CO}_2 = 95.4\%$ at a pressure of 1.967 bar and a temperature of 343.9 K compared to various models	27

3.10	Opacity data using the 2-3 mm-wavelength system for a mixture of $\text{SO}_2 = 84.7\%$ and $\text{CO}_2 = 0\%$ at a pressure of 0.033 bar and a temperature of 344.3 K compared to various models	27
3.11	Opacity data using the 2-3 mm-wavelength system for a mixture of $\text{SO}_2 = 3\%$ and $\text{CO}_2 = 96.5\%$ at a pressure of 0.944 bar and a temperature of 344.5 K compared to various models	28
3.12	Opacity data using the 2-3 mm-wavelength system for a mixture of $\text{SO}_2 = 1.4\%$ and $\text{CO}_2 = 98.4\%$ at a pressure of 2.007 bar and a temperature of 344.4 K compared to various models	28
3.13	Opacity data using the 2.7-4 mm-wavelength system for a mixture of $\text{SO}_2 = 84.7\%$ and $\text{CO}_2 = 0\%$ at a pressure of 0.101 bar and a temperature of 343.6 K compared to various models	29
3.14	Opacity data using the 2.7-4 mm-wavelength system for a mixture of $\text{SO}_2 = 9.1\%$ and $\text{CO}_2 = 89.2\%$ at a pressure of 0.936 bar and a temperature of 343.2 K compared to various models	29
3.15	Opacity data using the 2.7-4 mm-wavelength system for a mixture of $\text{SO}_2 = 4.2\%$ and $\text{CO}_2 = 95\%$ at a pressure of 2.016 bar and a temperature of 342.9 K compared to various models	30
3.16	Opacity data using the 2.7-4 mm-wavelength system for a mixture of $\text{SO}_2 = 84.7\%$ and $\text{CO}_2 = 0\%$ at a pressure of 0.060 bar and a temperature of 343.1 K compared to various models	30
3.17	Opacity data using the 2.7-4 mm-wavelength system for a mixture of $\text{SO}_2 = 5.5\%$ and $\text{CO}_2 = 93.5\%$ at a pressure of 0.927 bar and a temperature of 343.6 K compared to various models	31
3.18	Opacity data using the 2.7-4 mm-wavelength system for a mixture of $\text{SO}_2 = 2.5\%$ and $\text{CO}_2 = 97\%$ at a pressure of 2.004 bar and a temperature of 343.9 K compared to various models	31
4.1	Temperature as a function of altitude in the Venus atmosphere obtained using the Pioneer-Venus sounder and north probes	38
4.2	Pressure as a function of altitude in the Venus atmosphere obtained using the Pioneer-Venus sounder and north probes	38
4.3	A two dimensional graphic example of the ray-tracing process taken from Hoffman 2001 [18]. An off-nadir (left) and a limb sounding case (right) are shown. Two possible outcomes for the limb-sounding case are shown. d_3 shows the ray exiting the atmosphere, while d_c shows critical refraction.	44
4.4	Vector implementation of Snell's Law. Image courtesy of Hoffman 2001 [18]	48

4.5	Disk-averaged weighting function of the Venus atmosphere at frequencies of 8.42, 14.94, 22.46, and 86.1 GHz.	54
-----	--	----

CHAPTER I

INTRODUCTION

Active and passive microwave remote sensing techniques have been extensively used in the study of our sister planet, Venus. Unlike Earth's atmosphere, the Venus atmosphere is mostly comprised of gaseous carbon dioxide (CO_2). CO_2 comprises 96.5% of the atmosphere along with gaseous nitrogen (N_2) at about 3.5%. The Venus atmosphere has multiple trace constituents such as sulfur dioxide (SO_2), carbon monoxide (CO), water vapor (H_2O), carbonyl sulfide (OCS), and sulfuric acid vapor (H_2SO_4) [36].

Two sulfur-bearing compounds dominate the millimeter-wave emission from Venus: sulfur dioxide (SO_2) and gaseous sulfuric acid (H_2SO_4). At higher pressures H_2SO_4 thermally dissociates, forming H_2O and SO_3 , both of which exhibit relatively small amounts of microwave absorption at the abundance levels present in the Venus atmosphere. Thus, in the deep atmosphere, only SO_2 and CO_2 have the potential to affect the observed microwave emission.

Utilizing the millimeter-wavelength system at the Planetary Atmospheres Laboratory at Georgia Institute of Technology, it is possible to simulate the upper troposphere of Venus and take precise measurements of the millimeter-wavelength properties of sulfur dioxide. Using the measurements, a model that accurately predicts the opacity of sulfur dioxide in the Venus atmosphere has been verified. Applying this opacity model to a newly developed radiative transfer model makes it possible to determine the source of variations in the Venus millimeter-wavelength emission, such as were observed by Sagawa [32].

1.1 Background and Motivation

Radio absorptivity data from planetary atmospheres can be used to infer abundances of microwave absorbing constituents. Such data is obtained from entry probe radio signal absorption measurements, spacecraft radio occultation experiments, and Earth-based or spacecraft-based radio emission observations. This can only be done if reliable models for the microwave absorbing properties of potential constituents are available. The use of theoretically-derived microwave absorption properties for such atmospheric constituents, or models based on laboratory measurements taken under environmental conditions other than the atmosphere being studied, often leads to significant misinterpretation of the measured opacity data. Even if laboratory measurements have been already conducted, improvements in the sensitivity of microwave sensors may require higher precision laboratory measurements.

Using the measured millimeter-wavelength absorption spectra of SO₂ in a CO₂ atmosphere and the resulting opacity formalism, a radiative transfer model (RTM), has now been produced. The model can be applied to Earth-based and spacecraft-based radio emission measurements so as to provide planetary maps of SO₂ abundances at all altitudes of the Venus atmosphere. This model can be applied to Earth-based millimeter-wavelength observations of Venus so as to provide planetary maps of sulfuric acid vapor and sulfur dioxide abundances at and immediately below the main cloud layer. Interpretation of such observations will complement the study of long-term variations of SO₂ variations at the 70 km altitude level made with Venus-orbiting ultraviolet(uv) spectrometers [9].

It is well understood that the microwave emission spectrum of Venus reflects the abundance and distribution of its constituents. The most critical limiting factor in sensing these constituents is the knowledge of their microwave absorption properties under a Venus atmosphere. The millimeter-wavelength absorption of SO₂ at 94.1 GHz has been measured by Fahd and Steffes, [11]. Using newer technology it is possible to

measure more resonances with higher precision. Improved laboratory capabilities also allow for a wider range of environmental conditions, similar to those actually being probed, to be simulated. The millimeter-wavelength system used is able to reproduce conditions similar to those that exist on Venus. The centimeter-wave absorption spectra already measured by Steffes et al. [35] has been used to help choose a model that best represents the centimeter- and millimeter-wavelength opacity of SO_2 in a CO_2 atmosphere [3].

Sagawa [32] attributes the Venus millimeter-wavelength continuum brightness temperature variations to spatial variations in the abundances of both gaseous H_2SO_4 and SO_2 just below the cloud layer (48 km altitude). The developed RTM's weighting function confirms these results. Sagawa has also suggested that the effects of both constituents can be distinguished based on differences in frequency dependencies of their millimeter-wavelength opacities. However, to accomplish this, high accuracy models must be developed that characterize the opacity of each constituent and their frequency dependence. This thesis successfully characterizes SO_2 's absorption as a function of pressure, temperature, concentration, and frequency for both centimeter and millimeter-wavelengths.

1.2 Organization

The objective of this research has been to determine the absorption properties of gaseous sulfur dioxide in a carbon dioxide atmosphere at centimeter and millimeter wavelengths. The formalism identified from the results has been used to create a radiative transfer model (RTM) for Venus. The thesis is organized as follows:

Chapter 2 provides a discussion of the measurement techniques for the millimeter-wavelength opacity of a gas. A complete description of the measurement system used for this work is presented.

Chapter 3 describes the measurement uncertainties involved with the experimental setups. An explanation of the data sets used and the analysis process are included. Finally a model is proposed.

Chapter 4 describes the newly-developed radiative transfer model. A discussion on radiative transfer theory is presented followed by describing the necessary parameters. The correct formula for tracing a ray through different atmospheric layers as well as methods for making the RTM computationally efficient follows. Later there is a discussion on how to simulate an antenna beam by integrating a simulated antenna beam pattern into this RTM. Ending this chapter is the model's results compared to Venus observations.

Chapter 5 summarizes the results of this work and presents suggestions for further investigations. An overview on this work's impact on Venus observations is provided.

CHAPTER II

EXPERIMENT DESIGN, THEORY, AND RESULTS

Verifying the millimeter-wavelength absorption spectrum of SO_2 is important for the study of the atmosphere of Venus. Making measurements under simulated Venus conditions assures the accuracy of any model derived from such measurements. We describe the theory, laboratory equipment, measurement procedure, and derived uncertainties in the measurements of the millimeter-wavelength absorptivity of gaseous sulfur dioxide under simulated Venus conditions.

2.1 Measurement Theory

In this experimental program, the quality factor (Q) of a resonant mode of a resonator is used to measure the absorption of a gas or gas mixture [15]. The quality factor of a resonance is given by [25]

$$Q = \frac{2\pi f_0 \times \text{Energy Stored}}{\text{Average Power Loss}} \quad (2.1)$$

where f_0 is the resonant frequency. The Q of a resonance can be measured directly from f_0 by dividing it by its half-power bandwidth (HPBW).

$$Q = \frac{f_0}{HPBW} \quad (2.2)$$

The Q of a lossy gas (ϵ'/ϵ'') and its opacity are related by

$$\alpha \approx \frac{\epsilon''\pi}{\epsilon'\lambda} = \frac{1}{Q_{gas}} \frac{\pi}{\lambda} \quad (2.3)$$

where ϵ' and ϵ'' are the real and imaginary permittivity of the gas, λ is the wavelength in km, and α is the absorptivity of the gas in Nepers/km (1 Neper = 8.686 dB). Since

Q can be affected by more than just the gas added, the Q of the gas-filled resonator is given by

$$\frac{1}{Q_{loaded}^m} = \frac{1}{Q_{gas}} + \frac{1}{Q_r} + \frac{1}{Q_{ext1}} + \frac{1}{Q_{ext2}} \quad (2.4)$$

where Q_{loaded}^m is the measured quality factor of a resonance in the presence of a test gas, Q_{gas} is the quality factor of the gas under test, Q_r is the quality factor of the resonator in the absense of coupling losses, and Q_{ext1} and Q_{ext2} are the external coupling losses. Since the resonator used is symmetric, it is safe to assume $Q_{ext1} = Q_{ext2}$. Coupling losses can be derived from the transmissivity $t = 10^{-S/10}$, where S is the measured insertion loss of the resonator in decibels (dB) at the frequency of a particular resonance using the following relationship [25]

$$t = \left[2 \frac{Q^m}{Q_{ext}} \right]^2, \quad (2.5)$$

$$Q_{ext} = \frac{2Q^m}{\sqrt{t}} \quad (2.6)$$

Q_r is related to the measured Q at a vacuum by

$$\frac{1}{Q_{vac}^m} = \frac{1}{Q_r} + \frac{1}{Q_{ext1}} + \frac{1}{Q_{ext2}} \quad (2.7)$$

where Q_{vac}^m is the measured Q under vacuum conditions. Substituting equation 2.6 into equations 2.4 and 2.7 gives

$$\frac{1}{Q_{gas}} = \frac{1 - \sqrt{t_{loaded}}}{Q_{loaded}^m} - \frac{1 - \sqrt{t_{vac}}}{Q_{vac}^m} \quad (2.8)$$

where t_{loaded} and t_{vac} are the transmissivity of the resonance taken in loaded and vacuum conditions respectively. When gas is added to the resonator there is a shift in the center frequency corresponding to the refractive index of the test gas. Since the quality factor is reliant on the center frequency this will affect the comparison

between the two measurements, even if the gas being tested is lossless. This effect is called dielectric loading [4]. This effect can be corrected by performing additional measurements of the quality factor with a lossless gas present. Adding the lossless gas shifts the center frequency of the resonances, and by adding more or less gas the center frequency can be adjusted to be exactly the same as the lossy gas. These measurements are used in place of the vacuum measurements in equation 2.8 and by converting Nepers/km to dB/km equation 2.3 becomes

$$\alpha = 8.686 \frac{\pi}{\lambda} \left(\frac{1 - \sqrt{t_{loaded}}}{Q_{loaded}^m} - \frac{1 - \sqrt{t_{matched}}}{Q_{matched}^m} \right) dB/km \quad (2.9)$$

2.2 Millimeter-Wavelength Measurement System

The high-sensitivity millimeter-wavelength system used for measuring the opacity of gaseous sulfur dioxide under Venus conditions is similar to the one used by Devaraj and Steffes [8] [6]. The system is comprised of two subsystems for measuring different bands of the millimeter-wavelength spectrum (W-band/F-band). The simulator consists of a glass pressure chamber capable of withstanding up to 3 bars of pressure along with a temperature chamber capable of operating up to 400 K. The W-band subsystem is used for measurements in the 2.7-4.0 millimeter-wavelength range while the F-band system is used for the 2-3 millimeter-wavelength range. The following sections describe each subsystem and their components.

2.2.1 W-band Subsystem

The W-band measurement system is used to measure the 2.7-4.0 mm-wavelength properties of sulfur dioxide and shown in Figure 2.1.

A synthesized swept signal generator (HP 83650B) is used to generate a signal in the 12.5-18.3 GHz range which is fed to a times-six active multiplier chain (AMC) via low-loss, high frequency coaxial cables. The active multiplier then feeds the 75-110

GHz signals (swept over the range covered by each single resonance) to the Fabry-Perot resonator via WR-10 waveguides. The millimeter-wavelength radio frequency (RF) signal from the output port of the Fabry-Perot resonator (FPR) is fed via waveguide to a QuinStar Technology QMH series harmonic mixer. The local oscillator (LO) and the intermediate frequency (IF) are connected via an external diplexer. The harmonic mixer is locked to the 18th harmonic of the spectrum analyzer LO and is used in the “external mixer” mode with the spectrum analyzer (HP 8564E).

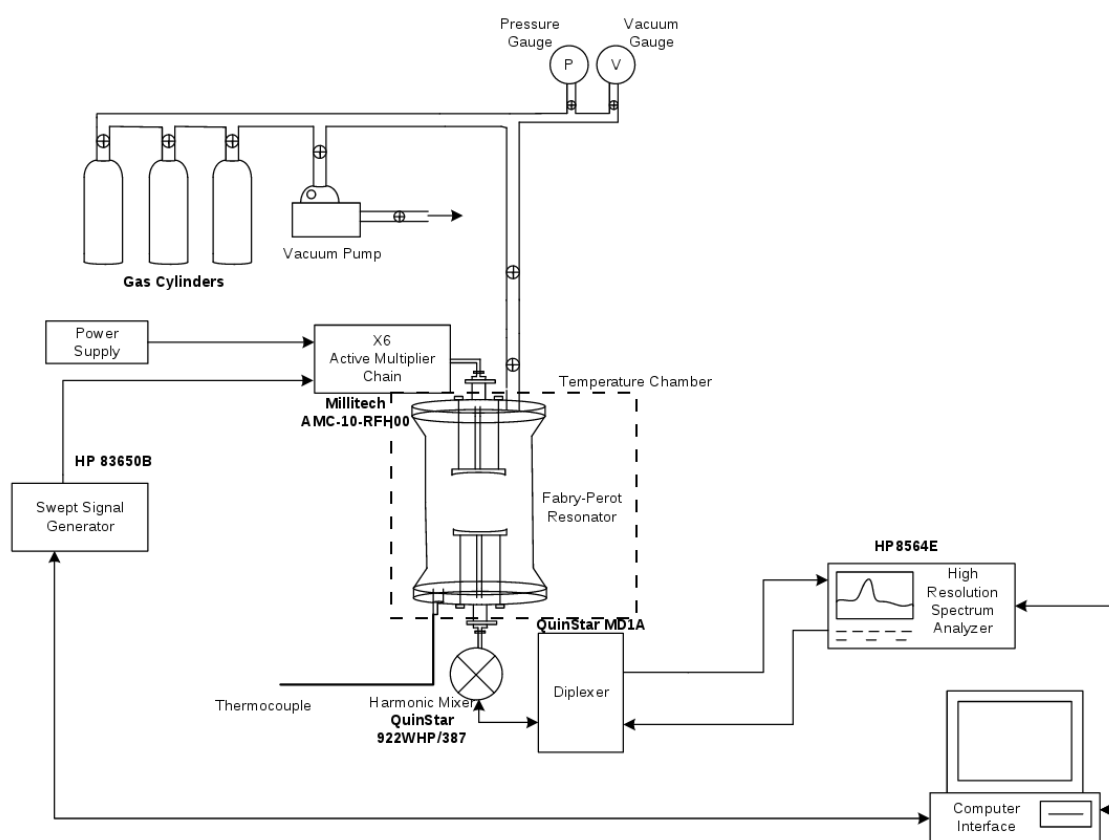


Figure 2.1: Block diagram of the W-band measurement system. Solid lines represent the electrical connections and the arrows show the direction of the signal propagation. Valves controlling the flow of gasses are shown by small crossed circles.

2.2.2 F-band Subsystem

The F-band measurement system is used to measure the 2-3 mm-wavelength properties of sulfur dioxide and is shown in figure 2.2.

The swept signal generator (HP 83650B) is used to generate a signal in the 33-50 GHz range which is amplified and fed through a frequency tripler. The output of the tripler is fed to the input of the FPR via WR-8 waveguides. The RF signal from the output port of the FPR is fed to a harmonic mixer which can operate with an LO frequency as high as 18 GHz. An external diplexer is used to combine the IF and LO signals. For a particular RF and IF frequency, the LO frequency can be computed using

$$f_{LO} = \frac{f_{RF} - f_{IF}}{N_H} \quad (2.10)$$

where N_H is the lowest integer such that $f_{lo} < 18$ GHzs.

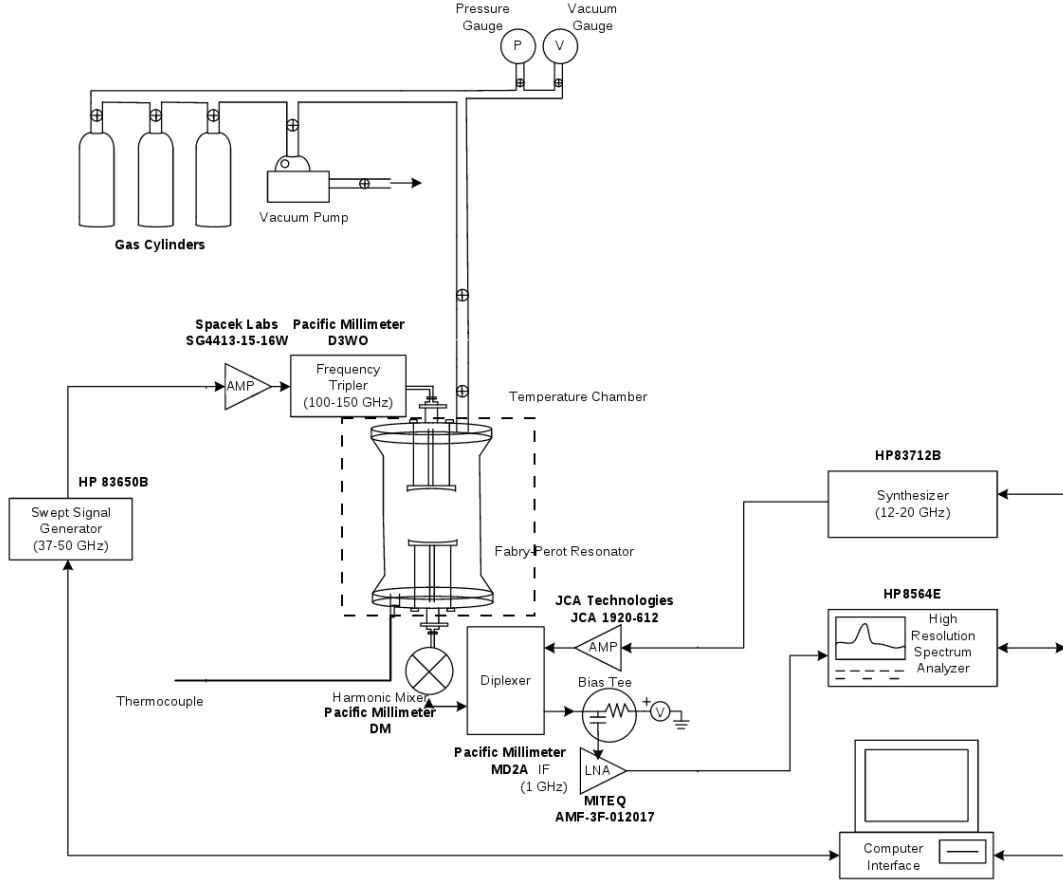


Figure 2.2: Block diagram of the F-band measurement system. Solid lines represent the electrical connections and the arrows show the direction of the signal propagation. Valves controlling the flow of gasses are shown by small crossed circles.

2.3 Data Handling Subsystem

The data acquisition system consists of a computer connected to the spectrum analyzer (HP 8564E), swept signal generator (HP 83650B), and continuous wave (CW) signal generator (HP 83712B, the local oscillator for the F-Band system) via a general purpose interface bus (GPIB). The instruments are controlled via Matlab script and their appropriate programming language. The software used is similar to Devaraj and Steffes [6, 8] with modifications for equipment changes.

2.4 *Measurement Procedure*

The most important prerequisite for performing measurement of gas properties is ensuring a leak-proof system. This is done through two methods, the first method is by drawing a vacuum inside the FPR and verifying the integrity of the vacuum over time. The second method is by adding a positive pressure of CO₂ to the system and making sure there are no leaks in any of the connectors and valves. Ensuring a leak-proof system allows for not only precise measurements but also ensures no toxic gases are released into the testing environment.

After the system is ensured to be leak-proof and at a stable temperature, a vacuum is drawn and a measurement is taken using the appropriate subsystem (W-band for 2.7-4.0 mm-wavelengths, F-band for 2-3 mm-wavelengths). This allows for a baseline measurement of the FPR's resonances and the Quality factor. Once this baseline is established the gas under test is added to the system.

Once the gas temperature has stabilized, another set of tests measuring the resonant frequencies along with the quality factors is taken. More gas is added and the procedure is repeated until measurements at all suitable pressures are taken. A vacuum is drawn once again but this time it is pumped overnight due to the possibility of adsorption (or "sticking") of the gas being tested (SO₂) to metal surfaces inside the vessel. This second vacuum measurement is taken to measure any possible system drift.

Once the second vacuum measurement is taken, CO₂ is then added to the chamber until the resonances are matched to the same frequency of our test gas (note that at the pressures and frequencies used for our experiment, pure CO₂ is essentially lossless). Again measurements are taken and this is repeated for every pressure of the test gas. Once completed a vacuum is again drawn and another test is taken.

Lastly the system is set up for a transmissivity test where we measure t (equation 2.5) for each given resonant frequency. This is done by passing the Fabry-Perot

resonator and connecting the input and output waveguides through a WR-10 20 dB directional coupler. The signal level is then measured and used to calculate t . The system is then set back up and is ready for a new test.

CHAPTER III

MODEL FITTING AND MODIFICATIONS

In total, 36 data sets were taken at 2-4 mm-wavelength and at two temperatures (12 at ~ 308 K and 24 at ~ 343 K). This, along with data taken at the centimeter-wavelength by Steffes et al. [35] (10 data sets at ~ 435 K, 10 data sets at ~ 490 K, and 5 data sets at ~ 550 K), were used in finding the best-fit model.

Before creating a new formalism for the absorption of SO_2 in a CO_2 atmosphere, analysis of previous models was conducted. The Van Vleck and Weisskopf Model (VVW) used by Fahd and Steffes [12] with the new JPL rotational line catalog (Pickett, et al. [31]) was found to fit 85.88% of all 500 data points within 2σ uncertainty (95% confidence). Consideration of the model analysis process and the final model are presented.

3.1 Measurement Uncertainties

There are five uncertainties for absorptivity measurements using the centimeter and millimeter wavelength systems (Hanley [14]) at the Planetary Atmospheres Laboratory at The Georgia Institute of Technology: instrumentation errors and electrical noise (Err_{inst}), errors in dielectric matching (Err_{diel}), errors in transmissivity measurement (Err_{trans}), errors due to resonance asymmetry (Err_{asym}), and errors in measurement conditions (Err_{cond}) resulting from uncertainties in temperature, pressure, and mixing ratio. The term Err is used for representing 2σ uncertainties.

Instrumental errors and electrical noise are due to the limited sensitivity of the electrical devices and their ability to accurately measure bandwidth ($BW_{measured}$) and the center frequency (f_o). Electrical noise arises from the limited-stability frequency references and the noise of the internal electronics. Electrical noise is uncorrelated

(with itself) and the best estimate of instrumental uncertainty is the variance of multiple measurements. The variance of the error estimate is given by the sample variance (S_N^2) weighted by the confidence coefficient (B) as

$$\sigma_N^2 = B \frac{S_N^2}{N_{samples}} \quad (3.1)$$

where $N_{samples}$ is the number of independent measurements of the sample. For the millimeter-wavelength system, five sets of independent measurements of each resonance are taken. A confidence coefficient (B) of 2.776 is used. This corresponds to the 95% confidence interval (2σ). The center frequency standard deviation is very small and its effect on the uncertainty in Q is negligible. Therefore, S_N is the sample standard deviation of the bandwidth of the measurements.

The HP 8564E spectrum analyzer is used for measuring the resonances in the millimeter-wavelength system. Its manufacturer-specified instrumental uncertainties are the 3σ values [16]. The 3σ standard deviation for the center frequency and bandwidth are estimated by

$$Err_o \leq \pm(f_o \times f_{ref\ acc} + 0.05 \times SPAN + 0.15 \times RBW + 10)(Hz) \quad (3.2)$$

$$Err_{BW} \leq \pm(BW_{measured} \times f_{ref\ acc} + 4 \times N_H + 2 \times LSD)(Hz) \quad (3.3)$$

where $f_{ref\ acc}$ is given as

$$f_{ref\ acc} = (aging \times time\ since\ calibration) + initial\ achievable\ accuracy \\ + temperature\ stability \quad (3.4)$$

and f_o , SPAN, RBW, N_H , and LSD are the center frequency, frequency span, resolution bandwidth, harmonic number, and least significant digit of the bandwidth measurement, respectively. LSD is calculated as

$$LSD = 10^x \quad (3.5)$$

where x is the the smallest positive integer value of x such that $SPAN < 10^{x+4}$. For $SPAN \leq 2 \text{ MHz} \times N_h$, Equation 3.2 becomes

$$Err_o \leq \pm(f_o \times f_{ref\ acc} + 0.01 \times SPAN + 0.15 \times RBW + 10)(Hz) \quad (3.6)$$

For the spectrum analyzer used, $f_{ref\ acc}$ reduces to

$$f_{ref\ acc} = (10^{-7} \times \text{years since calibrated}) + 3.2 \times 10^{-8} \quad (3.7)$$

The worst case scenario is used to transform the uncertainty in center frequency and bandwidth for both loaded and dielectrically matched measurements into an uncertainty in absorptivity as described in DeBoer and Steffes [5].

$$Err_{\Psi}^2 = \langle F_l^2 \rangle + \langle F_m^2 \rangle - \langle F_l F_m \rangle \quad (3.8)$$

where

$$\langle F_i^2 \rangle = \frac{\Upsilon_i^2}{f_{oi}^2} \left[\frac{Err_o^2}{Q_l^2} + Err_{BW}^2 + Err_{Ni}^2 + \frac{2Err_o Err_{BW}}{Q_i} \right], i = l, m \quad (3.9)$$

$$\langle F_l F_m \rangle = -\frac{\Upsilon_l \Upsilon_m}{f_{ol} f_{om}} \left[\frac{Err_o^2}{Q_i Q_m} + Err_{BW}^2 + \frac{Err_o Err_{BW}}{Q_l} + \frac{Err_o Err_{BW}}{Q_m} \right] \quad (3.10)$$

$$Q_i = \frac{f_{oi}}{f_{BW_i}}, i = l, m \quad (3.11)$$

$$\Upsilon_i = 1 - \sqrt{t}, i = l, m \quad (3.12)$$

where l and m denote loaded and dielectrically matched cases respectively and $f_{ol,om}$ and $f_{BWl,BWm}$ represent center frequency and bandwidth of loaded and dielectrically matched cases respectively. The 2σ uncertainty of the measured gas absorption due to instrumental errors and electrical noise is given by

$$Err_{inst} = \pm \frac{8.686\pi}{\lambda} Err_{\Psi} (dB/km) \quad (3.13)$$

where λ is the wavelength in km.

Errors in dielectric matching occur when the center frequency of the matched measurements are not precisely aligned with the center frequency of the loaded measurement. Since the Q of the resonator can vary slightly, this causes an uncertainty in the Q of the matched measurement at the true center frequency of the loaded measurement. The method used to calculate the magnitude of this effect is similar to Hanley [14]. While this error is the smallest due to the high precision of the software controlled matching, it is important to calculate and account for. The magnitude of this effect is calculated by comparing the Q of the three vacuum measurements to that of the dielectric matched measurements

$$\left(\frac{dQ}{df}\right)_i = \left|\frac{Q_{vac,i} - Q_{matched,i}}{f_{vac,i} - f_{matched,i}}\right| \text{ for } i = 1, 2, 3 \quad (3.14)$$

The maximum of the three values is used to calculate a dQ value

$$dQ = \left(\frac{dQ}{df}\right)_{max} \times |f_{loaded} - f_{matched}| \quad (3.15)$$

where f_{loaded} and $f_{matched}$ are the center frequencies of the resonances under loaded and matched conditions. The error in absorptivity due to imperfect dielectric matching is then computed by propagating $\pm dQ$ through Equation 2.9.

$$\begin{aligned} Err_{diel} = & \frac{8.686\pi}{\lambda} \\ & \times \left| \left(\frac{1 - \sqrt{t_{loaded}}}{Q_{loaded}^m} - \frac{1 - \sqrt{t_{matched}}}{Q_{matched}^m + dQ} \right) - \left(\frac{1 - \sqrt{t_{loaded}}}{Q_{loaded}^m} - \frac{1 - \sqrt{t_{matched}}}{Q_{matched}^m - dQ} \right) \right| \\ & (dB/km) \end{aligned} \quad (3.16)$$

Transmissivity errors are due to the uncertainties in the measurement amplitude. This is caused by variations in gains of losses of the millimeter-wavelength instruments (signal generators and spectrum analyzer), cables, adapters, and waveguides used in this system. This is done by taking multiple test measurements of signal loss through the system without the FPR and finding the standard deviation (S_N) of the signal

loss and weighing it by its confidence coefficient

$$Err_{msl} = \frac{4.303}{\sqrt{3}} S_N \quad (3.17)$$

For the millimeter-wavelength system, the signal level measurements involve sampling the RF power with a WR-10 20 dB directional coupler to feed the harmonic mixer for down-conversion and detection. While this ensures that the input to the harmonic mixer does not exceed its maximum allowed input power of -10 dBm, the WR-10 20dB directional coupler does not uniformly sample the input signal throughout the entire frequency range. To compensate for this, an additional 1.5 dB uncertainty is added to insertion loss error. The signal generator has a temperature stability of 1 dB/10° C, but an internal temperature equilibrium is reached after two hours [16]. Since the measurements units are stored at a constant temperature this uncertainty can be disregarded. The total uncertainty in insertion loss for the millimeter-wavelength system is calculated by

$$Err_{ins\ loss} = Err_{msl} + 1.5 \text{ (dB)} \quad (3.18)$$

The error in insertion loss is used to compute the transmissivity error

$$Err_{t,i} = \frac{1}{2} (10^{-S_i - Err_{ins\ loss}} - 10^{-S_i + Err_{ins\ loss}}), i = l, m \quad (3.19)$$

where l and m are the loaded and matched cases, respectively, and S is the insertion loss of the resonator. This is used to compute the 2σ uncertainties in opacity and is expressed as

$$Err_{trans} = \frac{8.686\pi}{2\lambda} \times \left| \left(\frac{\sqrt{t_l + Err_{t,l}} - \sqrt{t_l - Err_{t,l}}}{Q_{loaded}^m} - \frac{\sqrt{t_m - Err_{t,m}} - \sqrt{t_m + Err_{t,m}}}{Q_{matched}^m} \right) \right| \quad (dB/km). \quad (3.20)$$

Errors from asymmetry are due to the asymmetric nature of the resonances. These are more prominent at low temperatures and short wavelengths. Errors due to the asymmetry result from the disproportionate asymmetric broadening of the loaded measurements compared to the matched measurements. Equivalent full bandwidths based on assuming symmetry of the high and low sides of the resonances are calculated as

$$BW_{high} = 2 \times (f_{high} - f_{center}) \quad (3.21)$$

$$BW_{low} = 2 \times (f_{center} - f_{low}) \quad (3.22)$$

where BW_{high} , BW_{low} , f_{high} , f_{center} , and f_{low} are the high bandwidth, low bandwidth, higher frequency half power point, center frequency, and lower frequency half power point, respectively. For a perfectly symmetric resonance, $BW_{high} = BW_{low}$. The difference between the opacities calculated using BW_{high} and BW_{low} is defined as Err_{asym} and is calculated by

$$Err_{asym} = \frac{8.686\pi}{\lambda} \times \left| \left(\frac{1 - \sqrt{t_{loaded}}}{Q_{loaded,high}^m} - \frac{1 - \sqrt{t_{matched}}}{Q_{matched,high}^m} \right) - \left(\frac{1 - \sqrt{t_{loaded}}}{Q_{loaded,low}^m} - \frac{1 - \sqrt{t_{matched}}}{Q_{matched,low}^m} \right) \right| \quad (dB/km) \quad (3.23)$$

where $Q_{matched,high/low}^m$ and $Q_{loaded,high/low}^m$ are the measured Q's evaluated using the high and low bandwidths for loaded and matched cases.

The uncertainties in measured temperature, pressure, and concentration in the millimeter-wavelength system contribute to the total uncertainty due to the measurement conditions (Err_{cond}). While uncertainties in measurement conditions do not directly affect the measurements of millimeter-wavelength absorptivity, they still need to be accounted for when evaluating the opacity formalisms. It is computed by

$$Err_{cond} = \sqrt{Err_{temp}^2 + Err_p^2 + Err_c^2} (dB/km) \quad (3.24)$$

with Err_{temp} , Err_p , and Err_c representing the 2σ uncertainties in temperature, pressure, and concentration (or mole fraction) respectively. Each of these are calculated by taking the maximum modeled opacity with each uncertainty minus the minimum modeled opacity and halving the difference.

Temperature was measured using a T type thermocoupler along with a Wavetek 23XT voltmeter. The voltmeter has a temperature accuracy of $\pm(1\%+2^\circ C)$. Since the voltmeter has a cold compensation circuitry it is unnecessary to correct for ambient temperature. The temperature inside the test vessel is stable enough that it does not drift a significant amount during the hour it takes to run a test. The uncertainty in temperature is calculated by

$$T = T_{read} \pm (T_{read} \times 1\% + 2) \quad (3.25)$$

where T_{read} is the temperature (in $^\circ C$) displayed by the Wavetek 23XT voltmeter.

Pressure was measured using an Omega DPG-7000 which has an accuracy of $\pm 0.05\%FS$ (full scale). Since this pressure gauge measures pressure relative to ambient it is necessary to take a measurement before and after each test to ensure that the ambient pressure did not change significantly during the test. The average change in pressure during a test was at most 2 mbar. The cause of this change was identified as a change in ambient pressure during the test. Since the Omega DPG-7000 is a relative pressure gauge it was necessary to track ambient pressure. A vacuum was ensured by comparing the Omega DPG-7000 reading to that of an absolute pressure gauge (Druck DPI 104). The Druck has an accuracy of $\pm 0.05\%FS$ as well as a resolution of ± 1 mbar. The uncertainty in pressure reading is calculated by

$$P = P_{read} \pm (P_{FS} \times .05\% + 3) \quad (3.26)$$

where P_{FS} is the full scale pressure of the Omega DPG-7000 (3.08 bars).

Since Err_{cond} is dependent on the opacity model, this uncertainty is maintained

separately from Err_{tot} . Thus the total 95% confidence for the measurement uncertainty is expressed in dB/km as per Hanley [14]

$$Err_{tot} = \sqrt{Err_n^2 + Err_{diel}^2 + Err_{trans}^2 + Err_{asym}^2} \text{ (dB/km)}. \quad (3.27)$$

3.2 Model Analysis Process

The models considered in this comparison are the Van Vleck-Weisskopf model (using coefficients from Fahd and Steffes [12]) and the Ben-Reuven model as calculated by Suleiman et al. [37]. The comparison of these models are done using a L_2 norm analysis.

The following compliance function was used to calculate the number of data points that each model encompassed,

$$\mathbf{1}_{model}(\alpha) = \begin{cases} 1 & : |\alpha_{measured} - \alpha_{model}| \leq \sqrt{Err_{tot}^2 + Err_{cond}^2} \\ 0 & : |\alpha_{measured} - \alpha_{model}| > \sqrt{Err_{tot}^2 + Err_{cond}^2} \end{cases} \quad (3.28)$$

where $\mathbf{1}_{model}$ is the compliance function for each model, and $\alpha_{measured}$, α_{model} is the measured absorption and the calculated absorption, respectively. Err_{tot} and Err_{cond} are the systematic and conditional errors as described previously. The percentage of data points that each model encompasses can be calculated using,

$$Per_{model} = \frac{\sum_{i=1}^N \mathbf{1}_{model}(\alpha_i)}{N} \times 100\% \quad (3.29)$$

where Per_{model} is the percentage of data points that the model fits and N is the total number of data points. The final results are summarized in Table 1.

Table 1: The percentage of the measured data points within 2σ uncertainty of the different models

SO ₂ opacity model	Centimeter-Wavelength (1-8 GHz)	Millimeter-Wavelength (80-150 GHz)	Total
Fahd and Steffes (1992)	82.95%	88.89%	84.49%
Suleiman (1997)	62.98%	88.10%	70.37%

3.3 Experimental Results

High accuracy laboratory measurements of the temperature and pressure dependence of the millimeter-wavelength absorption of gaseous SO_2 in a CO_2 atmosphere have been conducted at 308K and 345 K and at pressures from 30 mbar to 3 bars for wavelengths between 2-4 millimeters. The following plots show the results of these absorptivity measurements with the accompanying 2σ uncertainties. For comparison purposes these plots also show two known formalisms of SO_2 's absorptivity. One developed by Suleiman et al. 1997 [36] and the second by Fahd and Steffes [11] but using the new JPL line catalog [31].

3.3.1 Accuracy of Constituents

It is necessary to ensure that the gases used in each experiment are correctly characterized. Initially the bottle of SO_2 was assumed to consist of 100% SO_2 . The bottle was sent to Airgas® for analysis. It was concluded that the SO_2 bottle used was actually comprised of 84.7% SO_2 and 15.3% N_2 . Since N_2 has no absorptivity at centimeter and millimeter-wavelengths it can be safely disregarded. Thus, the SO_2 and CO_2 mole fractions do not add up to 100% in the following plots.

The CO_2 tank used was the same tank used in Steffes et al. [35]. Since the CO_2 absorption measured in that paper matched the previously published formalism for opacity and refractive index of CO_2 [17], it can be assumed that the tank contained pure CO_2 .

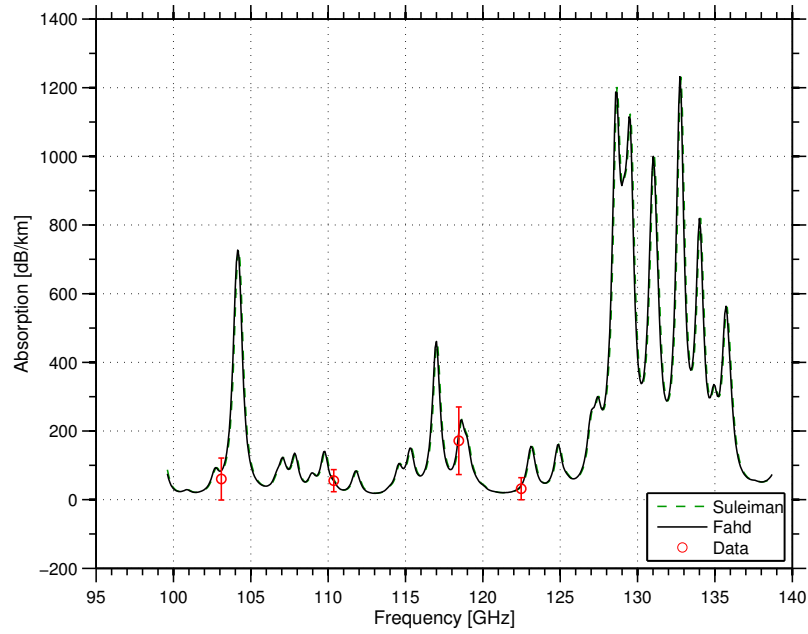


Figure 3.1: Opacity data using the 2-3 mm-wavelength system for a mixture of $\text{SO}_2 = 84.7\%$, $\text{CO}_2 = 0\%$ at a pressure of 0.030 bar and a temperature of 308.8 K compared to various models

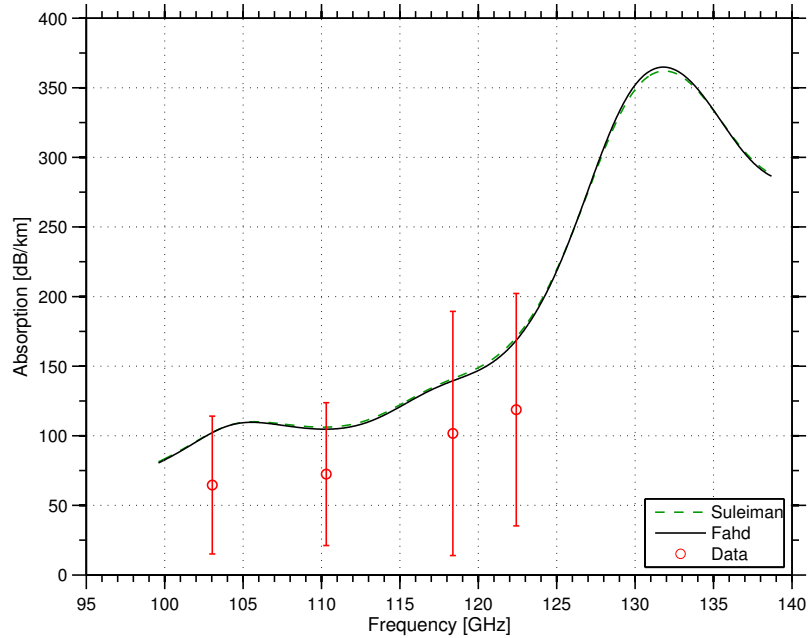


Figure 3.2: Opacity data using the 2-3 mm-wavelength system for a mixture of $\text{SO}_2 = 2.6\%$, $\text{CO}_2 = 96.9\%$ at a pressure of 0.970 bar and a temperature of 308.5 K compared to various models

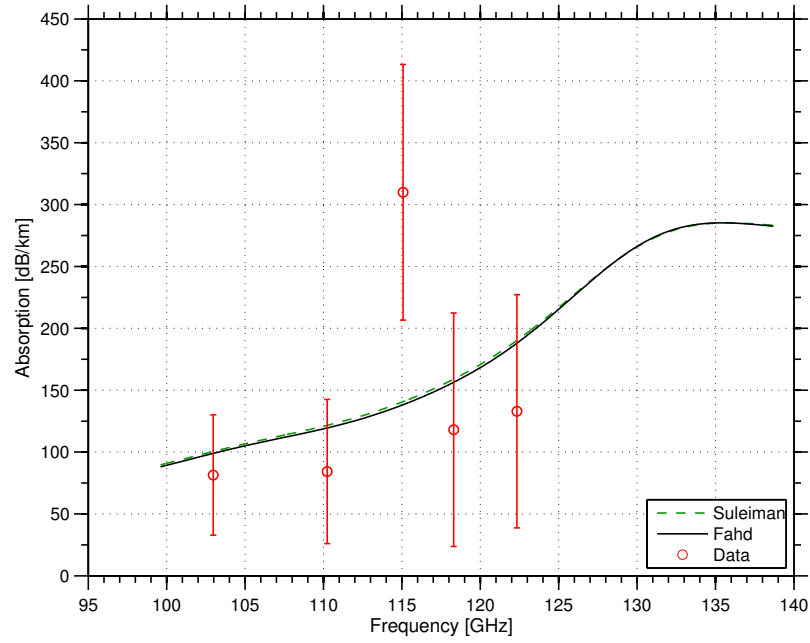


Figure 3.3: Opacity data using the 2-3 mm-wavelength system for a mixture of $\text{SO}_2 = 1.3\%$, $\text{CO}_2 = 98.5\%$ at a pressure of 1.995 bar and a temperature of 308.6 K compared to various models

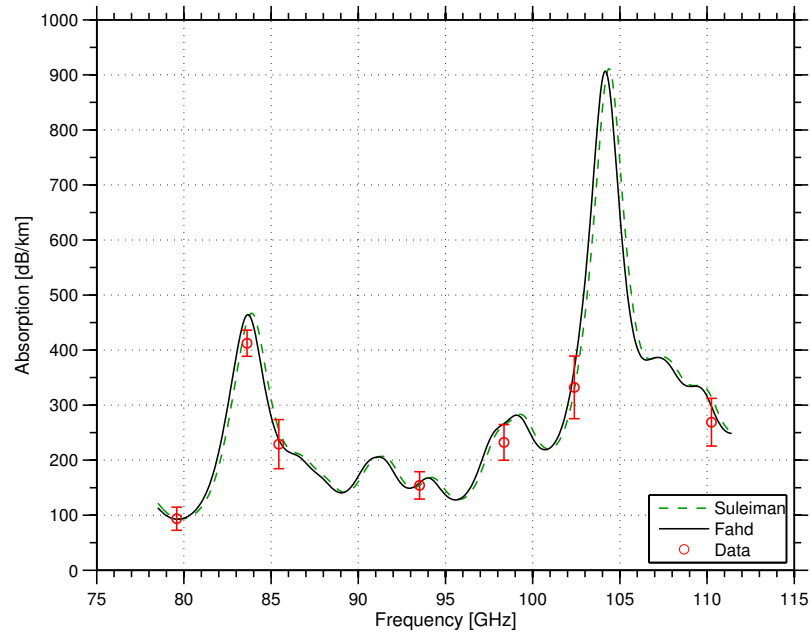


Figure 3.4: Opacity data using the 3-4 mm-wavelength system for a mixture of $\text{SO}_2 = 84.7\%$, $\text{CO}_2 = 0\%$ at a pressure of 0.116 bar and a temperature of 307.5 K compared to various models

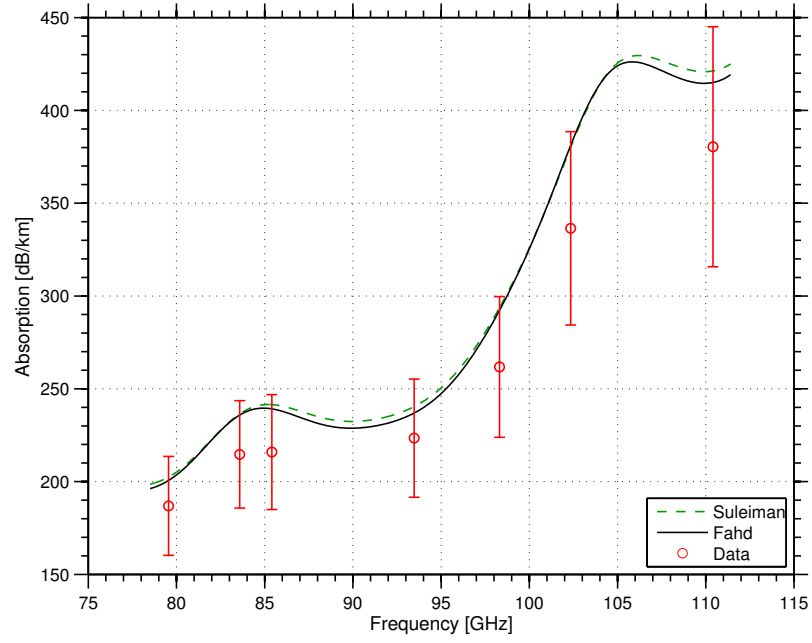


Figure 3.5: Opacity data using the 2.7-4 mm-wavelength system for a mixture of $\text{SO}_2 = 10.4\%$, $\text{CO}_2 = 87.7\%$ at a pressure of 0.943 bar and a temperature of 307.2 K compared to various models

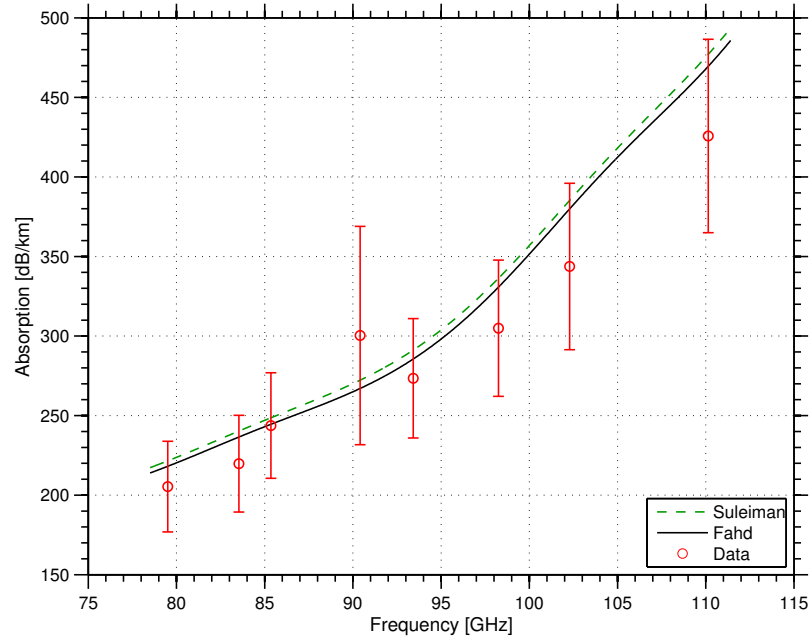


Figure 3.6: Opacity data using the 2.7-4 mm-wavelength system for a mixture of $\text{SO}_2 = 4.9\%$ and $\text{CO}_2 = 94.2\%$ at a pressure of 1.987 bar and a temperature of 307.2 K compared to various models

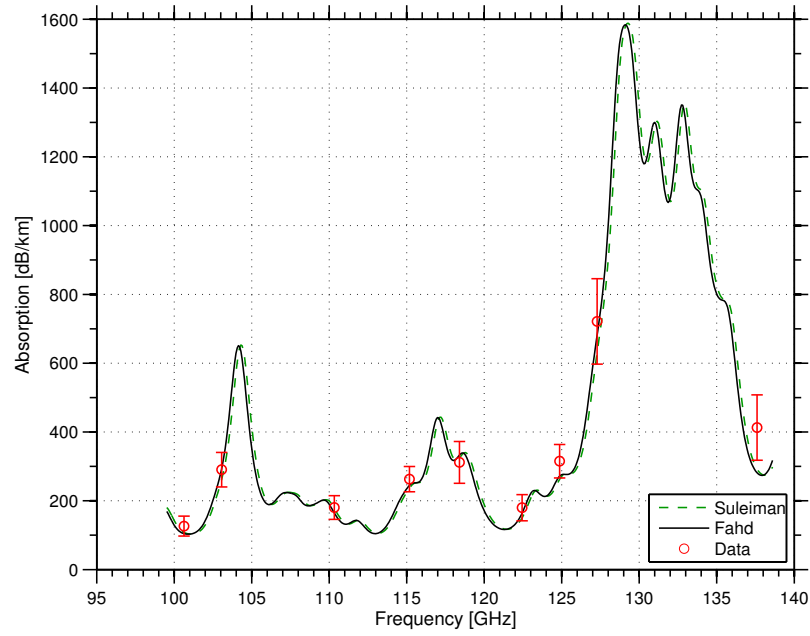


Figure 3.7: Opacity data using the 2-3 mm-wavelength system for a mixture of $\text{SO}_2 = 84.7\%$ and $\text{CO}_2 = 0\%$ at a pressure of 0.090 bar and a temperature of 344.4 K compared to various models

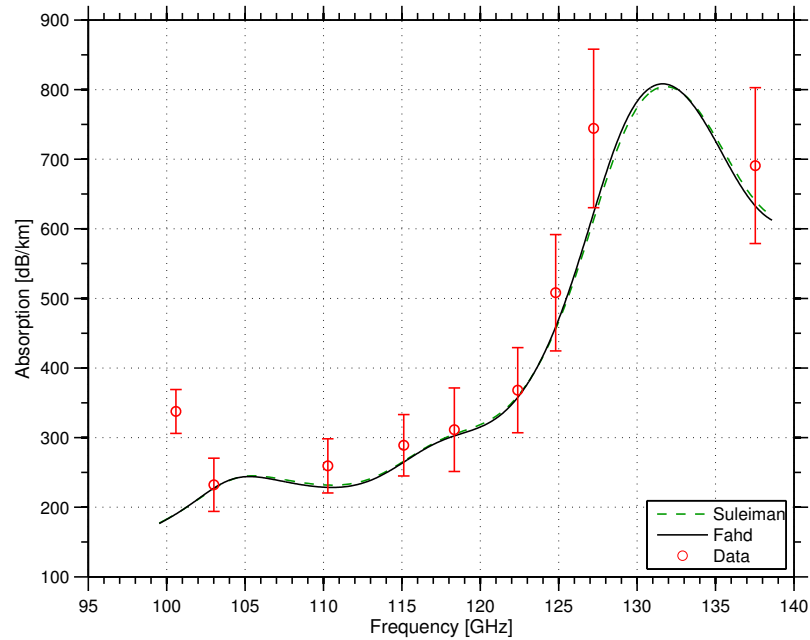


Figure 3.8: Opacity data using the 2-3 mm-wavelength system for a mixture of $\text{SO}_2 = 8.3\%$ and $\text{CO}_2 = 90.2\%$ at a pressure of 0.923 bar and a temperature of 344.6 K compared to various models

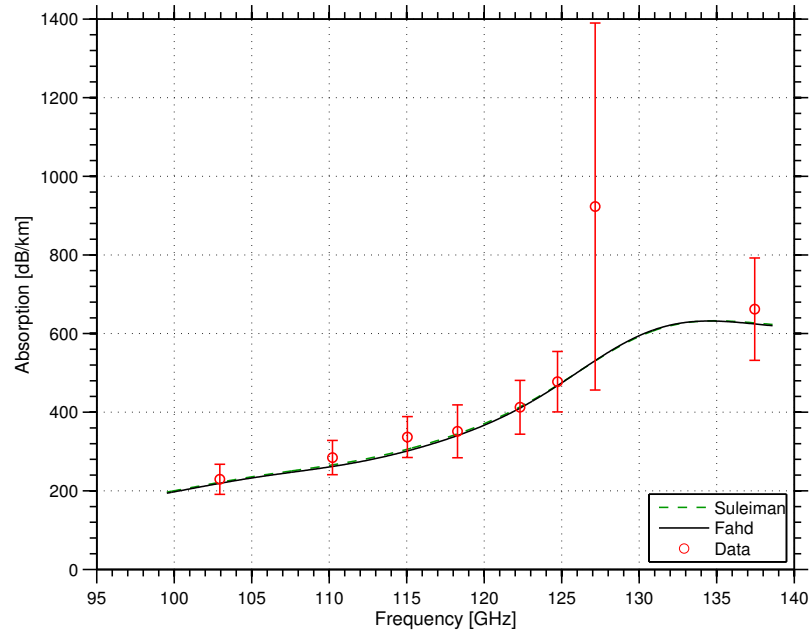


Figure 3.9: Opacity data using the 2-3 mm-wavelength system for a mixture of $\text{SO}_2 = 3.9\%$ and $\text{CO}_2 = 95.4\%$ at a pressure of 1.967 bar and a temperature of 343.9 K compared to various models

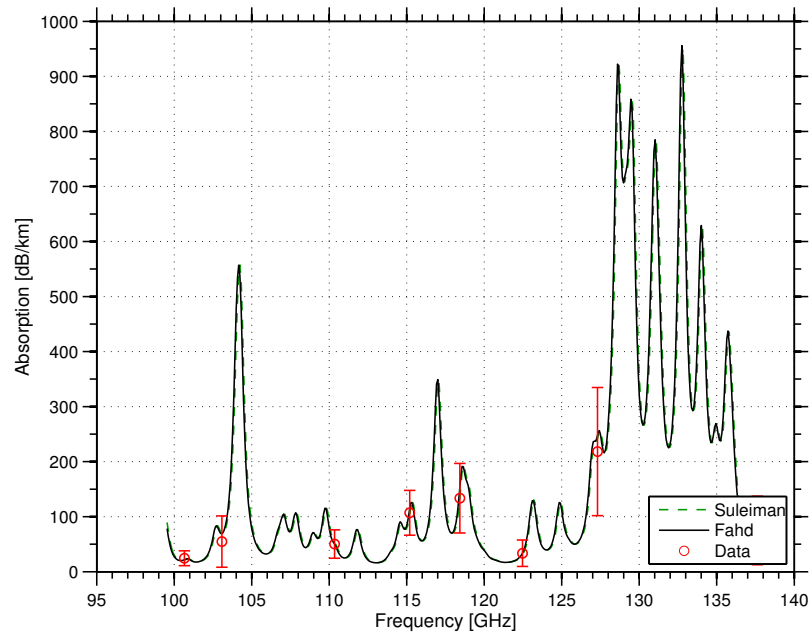


Figure 3.10: Opacity data using the 2-3 mm-wavelength system for a mixture of $\text{SO}_2 = 84.7\%$ and $\text{CO}_2 = 0\%$ at a pressure of 0.033 bar and a temperature of 344.3 K compared to various models

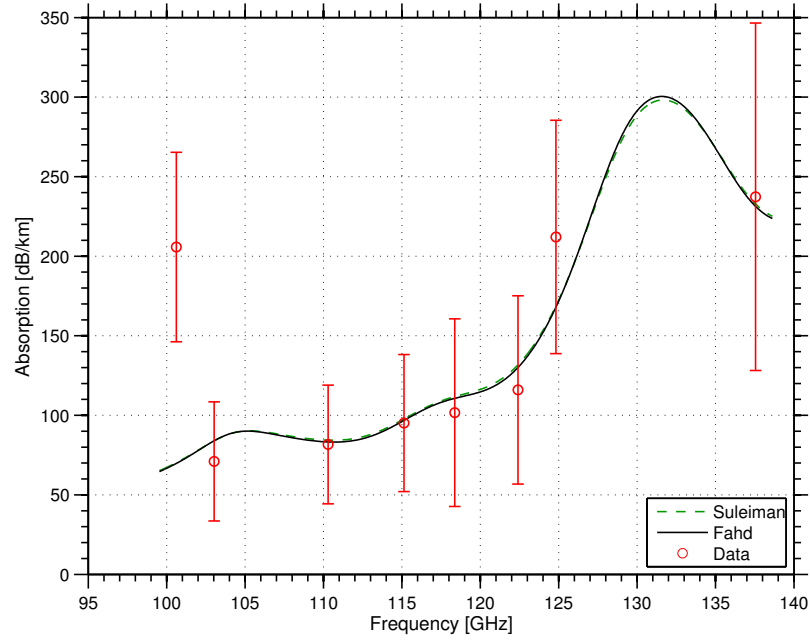


Figure 3.11: Opacity data using the 2-3 mm-wavelength system for a mixture of $\text{SO}_2 = 3\%$ and $\text{CO}_2 = 96.5\%$ at a pressure of 0.944 bar and a temperature of 344.5 K compared to various models

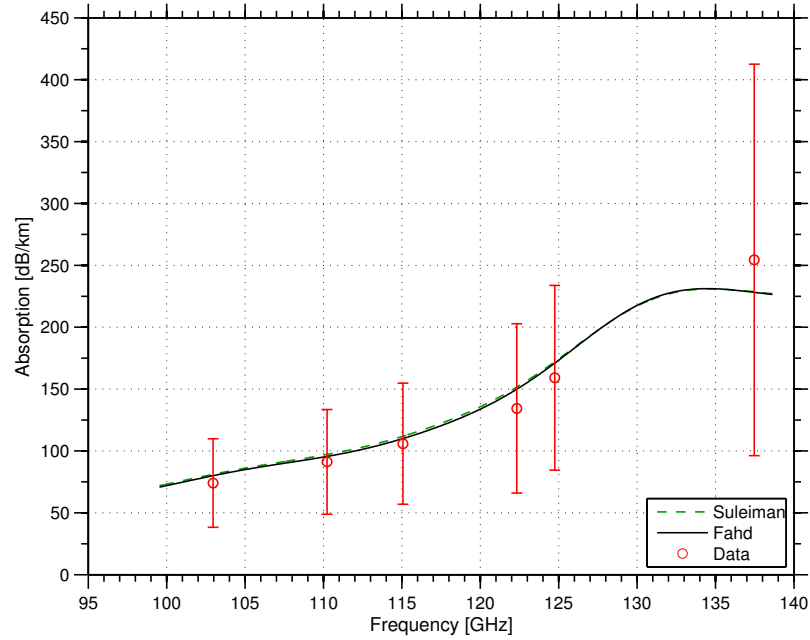


Figure 3.12: Opacity data using the 2-3 mm-wavelength system for a mixture of $\text{SO}_2 = 1.4\%$ and $\text{CO}_2 = 98.4\%$ at a pressure of 2.007 bar and a temperature of 344.4 K compared to various models

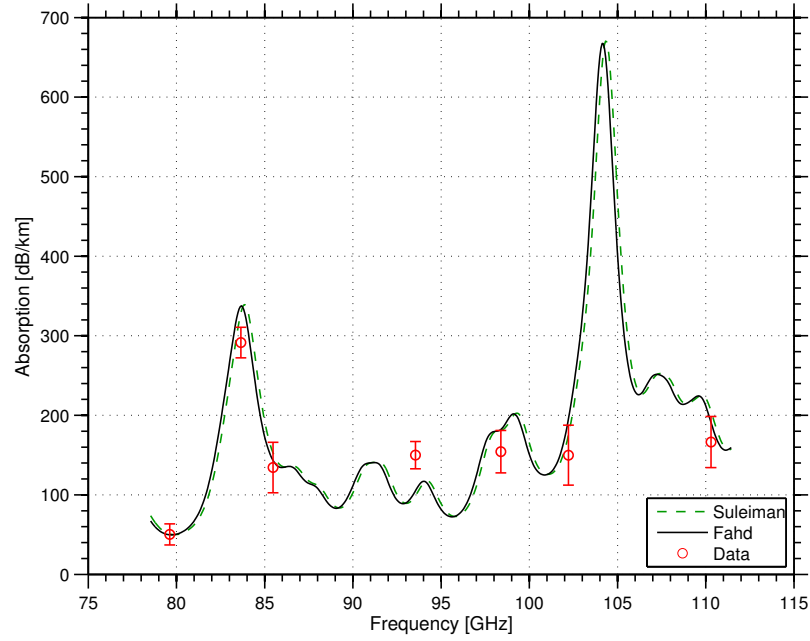


Figure 3.13: Opacity data using the 2.7-4 mm-wavelength system for a mixture of $\text{SO}_2 = 84.7\%$ and $\text{CO}_2 = 0\%$ at a pressure of 0.101 bar and a temperature of 343.6 K compared to various models

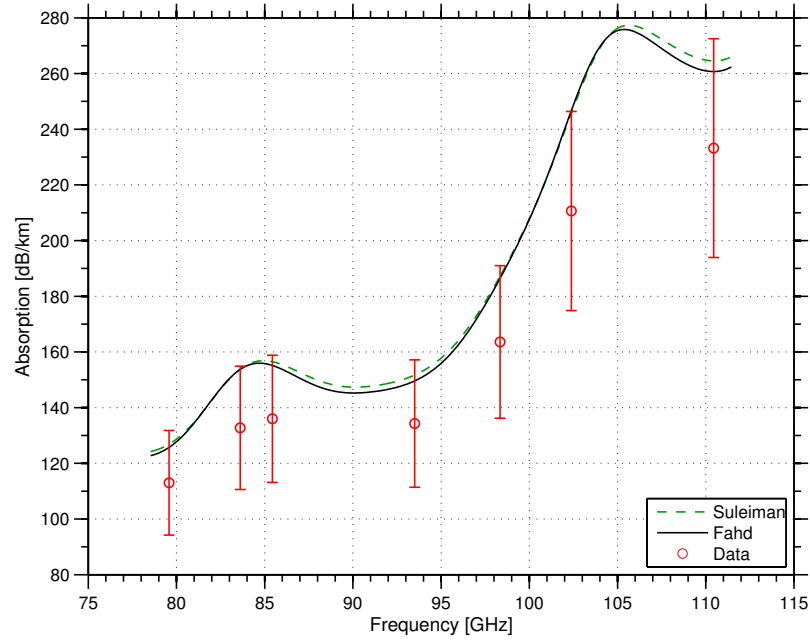


Figure 3.14: Opacity data using the 2.7-4 mm-wavelength system for a mixture of $\text{SO}_2 = 9.1\%$ and $\text{CO}_2 = 89.2\%$ at a pressure of 0.936 bar and a temperature of 343.2 K compared to various models

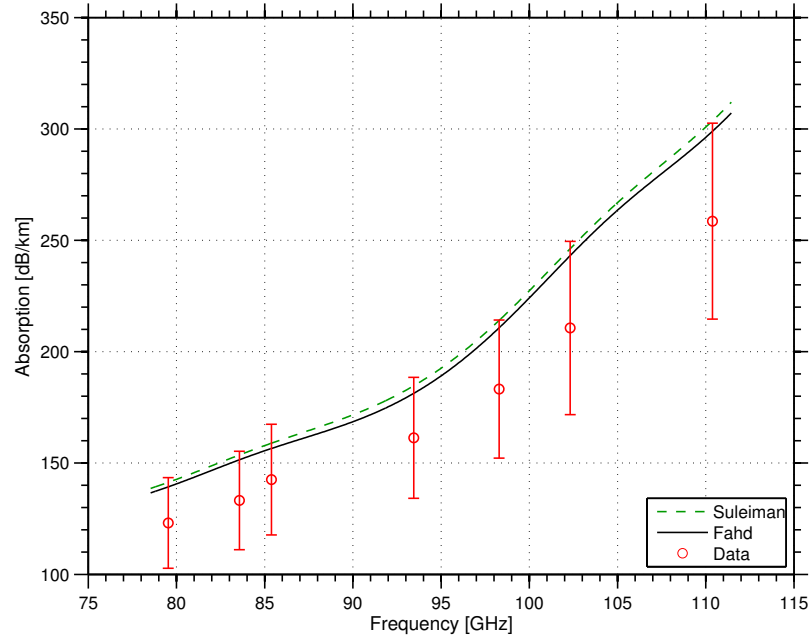


Figure 3.15: Opacity data using the 2.7-4 mm-wavelength system for a mixture of $\text{SO}_2 = 4.2\%$ and $\text{CO}_2 = 95\%$ at a pressure of 2.016 bar and a temperature of 342.9 K compared to various models

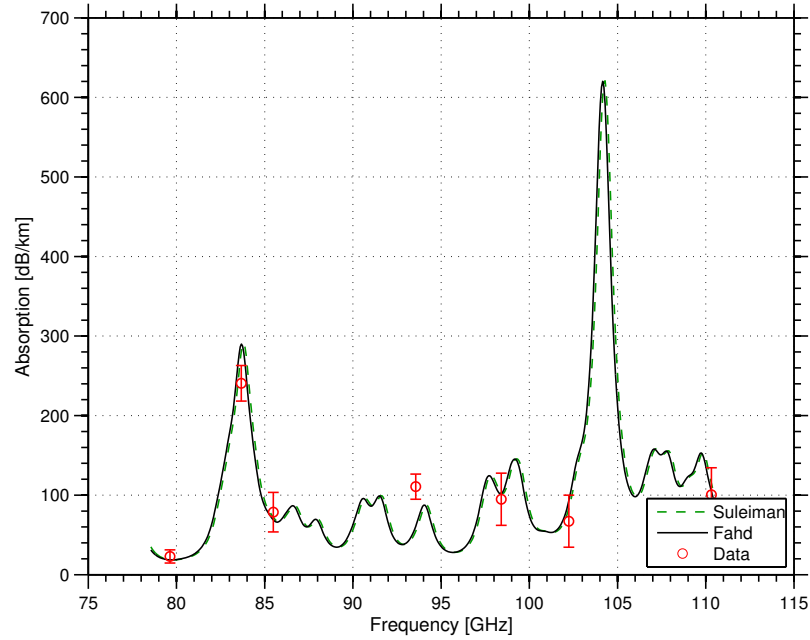


Figure 3.16: Opacity data using the 2.7-4 mm-wavelength system for a mixture of $\text{SO}_2 = 84.7\%$ and $\text{CO}_2 = 0\%$ at a pressure of 0.060 bar and a temperature of 343.1 K compared to various models

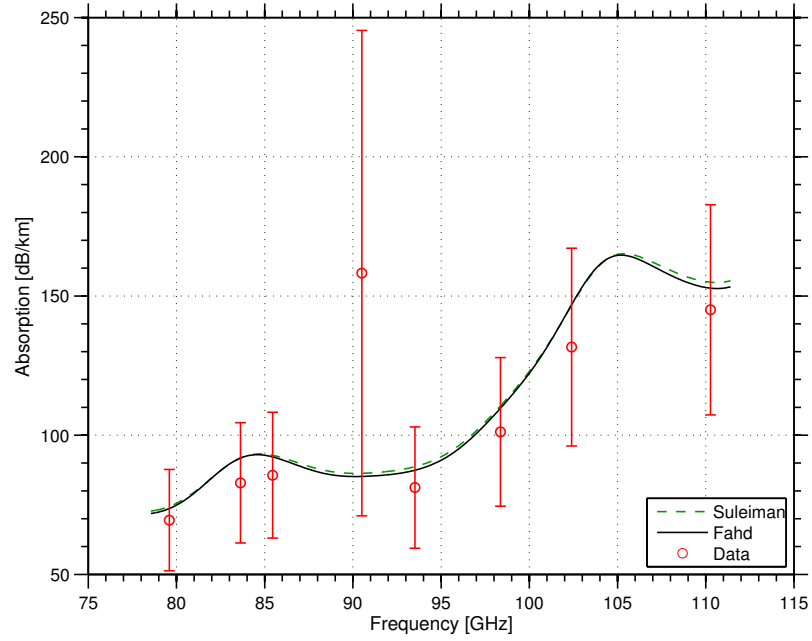


Figure 3.17: Opacity data using the 2.7-4 mm-wavelength system for a mixture of $\text{SO}_2 = 5.5\%$ and $\text{CO}_2 = 93.5\%$ at a pressure of 0.927 bar and a temperature of 343.6 K compared to various models

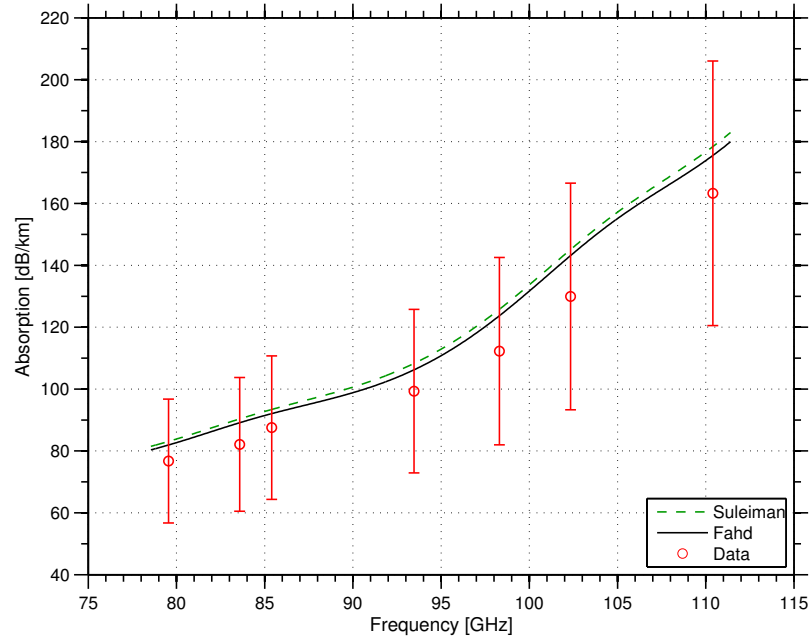


Figure 3.18: Opacity data using the 2.7-4 mm-wavelength system for a mixture of $\text{SO}_2 = 2.5\%$ and $\text{CO}_2 = 97\%$ at a pressure of 2.004 bar and a temperature of 343.9 K compared to various models

3.4 *Suggested Model*

Results indicate that the models for the centimeter- and millimeter-wavelength opacity from SO₂ in a CO₂ atmosphere by Suleiman et al. [37] and Fahd and Steffes [12] are both valid over the entire centimeter-and millimeter-wavelength range under simulated conditions for the upper atmosphere of Venus. Based on the percentage of data consistent with the models, we suggest the model from Fahd and Steffes [11], but using the updated line catalog from Pickett et al. [31]. This model employs the Van Vleck-Weisskopf lineshape, and was developed from measurements of SO₂/CO₂ mixtures conducted at room temperature. As per their paper, we employ only the rotational line catalog to compute opacity. (JPL spectral line catalog, Pickett et al., [31]). While both models perform well, the Fahd and Steffes [12] model appears to provide a slightly better fit to the overall data set.

It should also be noted that because both models were derived from measurements conducted at pressures of 6 bars or less, no allowance for the compressibility of CO₂ is included in these models. When performing the best-fit analysis of high-pressure data [35], a correction factor for compressibility was computed and entered into the models (by simply dividing the measured partial pressure of CO₂ by the compressibility, Z).

CHAPTER IV

RADIATIVE TRANSFER MODEL OF THE VENUS ATMOSPHERE

One key aspect of this research has been to model the microwave and millimeter-wave emission spectra from the surface of Venus and its atmosphere. This is accomplished using a radiative transfer model. The radiative transfer model (RTM) computes the brightness temperature of Venus for a given distribution of atmospheric constituents. The developed RTM is written in a modular way such that any input can be easily changed without changing other aspects. The RTM has the ability to simulate pencil-beam emissions, disk averaged emissions, or the emission over a selected antenna pattern.

4.1 Theoretical Background

The emission from the surface of Venus and its atmosphere can be computed using a Radiative Transfer Model (RTM). Radiative transfer is a method to solve for the emission of electromagnetic energy from a medium. In a most basic RTM, it is assumed that the solution for intensity (or brightness temperature) is computed from emissions along an infinitely thin beam (pencil beam). A second assumption is that the atmosphere is in local thermodynamic equilibrium (LTE). LTE implies that for a given moment or snapshot in time the atmosphere is static; that is, the model does not consider atmospheric dynamics when solving the radiative transfer equation. The differential form of the radiative transfer equation is

$$dI_\nu = -\alpha I_\nu ds + \alpha J ds \tag{4.1}$$

where dI_ν is the change in intensity at a given frequency ν over a path length ds , α is the absorption coefficient or attenuation over a path length ds , and J is the source function [23].

In the microwave and millimeter wave regime, effects from scattering approach the Rayleigh limit, and may be neglected without introducing significant error. Therefore the source function J becomes the Plank function.

$$J_\nu = B_\nu(T) = \frac{h\nu^3}{c^2} \frac{1}{\exp(\frac{h\nu}{kT}) - 1} \approx \frac{2kT\nu^2}{c^2} \quad (4.2)$$

where T is the temperature in Kelvin, h is Planck's constant, k is Boltzman's constant, and c is the speed of light (Karpowicz [20]). The approximation in equation 4.2 is for cases where $h\nu \ll kT$ (characteristic of centimeter and millimeter-wavelengths) and is known as the Rayleigh-Jeans approximation.

If equation 4.1 is integrated over the path s it becomes

$$I_\nu(s) = I_{\nu,o}(s_0)e^{-\tau_\nu(s_0)} + \int_0^{s_0} \alpha_\nu(s)B_\nu(T)e^{-\tau_\nu(s)}ds \quad (4.3)$$

where the first term is the intensity at the boundary of the integration and represents contributions to emissions from sources other than those over the path of integration, such as background or surface emission and τ is the optical depth defined by

$$\tau_\nu(s) = \int_0^s \alpha_\nu(s')ds' \quad (4.4)$$

For the terrestrial inner planets, the surface term is

$$I_{\nu,o}(s_0) = I_{surf} + I_{cmb} + I_{down} \quad (4.5)$$

where the first term (I_{surf}) is the surface emission, the second term (I_{cmb}) is the cosmic microwave background, and the final term (I_{down}) is the downwelling radiation from each atmospheric layer.

While intensity is a quantity often used in solar and ultra-violet remote sensing, it is far more common to use brightness temperature for longer wavelengths such

as infrared and microwave. This quantity is found by taking the approximation in Equation 4.2 and solving for T . Brightness temperature is defined as,

$$T_b = \frac{Tc^2}{2\nu k} \quad (4.6)$$

Substituting Equations 4.2, 4.6, and 4.5 into 4.3, and solving for brightness temperature, the equation for radiative transfer becomes,

$$\begin{aligned} T_b(\nu) = & \left(\epsilon(\theta)T_{surf} + [1 - \epsilon(\theta)]e^{-\tau_\nu(s)}T_{cmb} + T_{down}(\nu) \right) e^{-\tau_\nu(s_0)} \\ & + \int_0^{s_0} \alpha_\nu(s)T(s)e^{-\tau_\nu(s)}ds \end{aligned} \quad (4.7)$$

Where $\epsilon(\theta)$ is the surface emissivity, θ is the transmission angle upward, T_{surf} is the physical surface temperature, T_{cmb} is the cosmic background radiation temperature (2.7K) attenuated while going through the atmosphere (s), T is the physical temperature along the integration path, and finally $T_{down}(\nu)$ is the downwelling radiation from each atmospheric layer attenuated by every layer below it which is expressed as

$$T_{down}(\nu) = \int_{s_0}^0 \alpha_\nu(s)T(s)e^{-\tau_\nu(s)} \quad (4.8)$$

The discrete form of 4.7 can be expressed as,

$$\begin{aligned} T'_\nu(a) = & \epsilon(\theta)T_{surf}e^{-\tau_{0 \rightarrow \infty}} \\ & + [1 - \epsilon(\theta)]T_{cmb}e^{-2\tau_{0 \rightarrow \infty}} \\ & + \sum_{i=1}^N T_i(1 - e^{-\tau_i})[1 - \epsilon(\theta)]e^{-\tau_{0 \rightarrow i-1}}e^{-\tau_{0 \rightarrow \infty}} \\ & + \sum_{i=1}^N T_i(1 - e^{-\tau_i})e^{-\tau_{i+1 \rightarrow \infty}} \end{aligned} \quad (4.9)$$

where a is the impact parameter which describes how the ray is emitted from the planet and is computed using a Ray Tracing algorithm and $\tau_{j \rightarrow k}$ is the optical depth from layer j to layer k ,

$$\tau_{j \rightarrow k} = \sum_{i=j}^k \tau_i \quad (4.10)$$

τ_i is the optical depth of layer i and is given by

$$\tau_i = \int_{s(z=z_i)}^{s(z=z_{i+1})} \alpha(s) ds \quad (4.11)$$

where z_i is the height of the i^{th} layer [19].

To compute the surface emissivity ϵ the following formula can be used

$$\epsilon(\theta) = 1 - R_{surf}(\theta) \quad (4.12)$$

where

$$\begin{aligned} R_{surf}(\theta) = & \frac{1}{2} \left[\frac{\cos \theta - \sqrt{\epsilon_d/\eta_1^2 - \sin^2 \theta}}{\sin \theta + \sqrt{\epsilon_d/\eta_1^2 - \sin^2 \theta}} \right]^2 \\ & + \frac{1}{2} \left[\frac{\epsilon_d/\eta_1^2 \cos \theta - \sqrt{\epsilon_d/\eta_1^2 - \sin^2 \theta}}{\epsilon_d/\eta_1^2 \cos \theta + \sqrt{\epsilon_d/\eta_1^2 - \sin^2 \theta}} \right]^2 \end{aligned} \quad (4.13)$$

where θ is the transmission angle upward through the first atmospheric layer and η_1 is the index of refraction for the first atmospheric layer [19]. The dielectric constant of the surface ϵ_d is assumed to have a uniform value of 4.0 [30].

If Equation 4.9 is integrated over all angles of emission and divided by the number of samples taken, the disk-averaged brightness can be obtained. This is useful in comparing the model to full-disk observations made of Venus as well as producing residual plots of the planet. The residual plots can be used to find any discrepancies in the Venus atmosphere and allow for identification of atmospheric phenomenon.

It is also useful to know how each layer of the atmosphere affects the brightness temperature; this can be found through calculation of the weighting function,

$$W_i = (1 - e^{\tau_i})e^{-\tau_{i+1} \rightarrow N} \quad (4.14)$$

4.2 *Parameters of the Radiative Transfer Model*

The input parameters of the radiative transfer model (RTM) are the opacity formalisms for the various atmospheric constituents, the index of refraction for each atmospheric layer, the temperature-pressure profiles, and the vertical abundance profiles

for the absorbing constituents. Together the last two make up the Thermo-Chemical model of the atmosphere.

4.2.1 Temperature-Pressure Profiles

The temperature-pressure profiles for the atmosphere of Venus have been obtained from the data collected using the Pioneer-Venus sounder and north probes [33]. Figure 4.1 shows the temperature as a function of altitude in the Venus atmosphere as reported by the Pioneer-Venus sounder and north probes. Figure 4.2 shows the pressures as a function of altitude in the Venus atmosphere as reported by the Pioneer-Venus sounder and north probes.

The sounder probe temperature represents the temperature-pressure profile in the equatorial region of the Venus atmosphere. It is used for latitudes between -45° and $+45^\circ$. The north probe is representative of the polar regions of Venus and it used between $\pm 45^\circ$ and $\pm 90^\circ$. A physical surface temperature of 730 K is assumed in this RTM.

4.2.2 Opacity Formalisms

There are several major absorbing constituents at the microwave and millimeter-wave frequencies in the Venus atmosphere. The major constituents are gaseous CO_2 , N_2 , SO_2 , and H_2SO_4 , and liquid H_2SO_4 in the form of clouds. The formalisms used in this RTM are described below.

Gaseous $\text{CO}_2\text{-N}_2$

Although CO_2 is a non-polar molecule, collision induced absorption by gaseous CO_2 [1] is the dominate source of centimeter- and millimeter-wavelength absorption at low altitudes of the Venus atmosphere. The opacity from gaseous CO_2 and N_2 was derived by Ho et al. [17] based on their laboratory measurements of gaseous CO_2 and

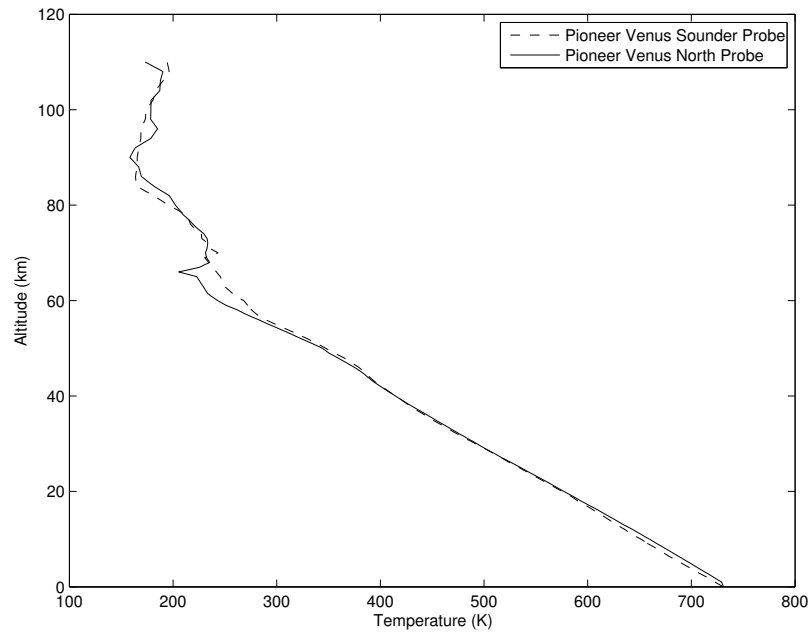


Figure 4.1: Temperature as a function of altitude in the Venus atmosphere obtained using the Pioneer-Venus sounder and north probes

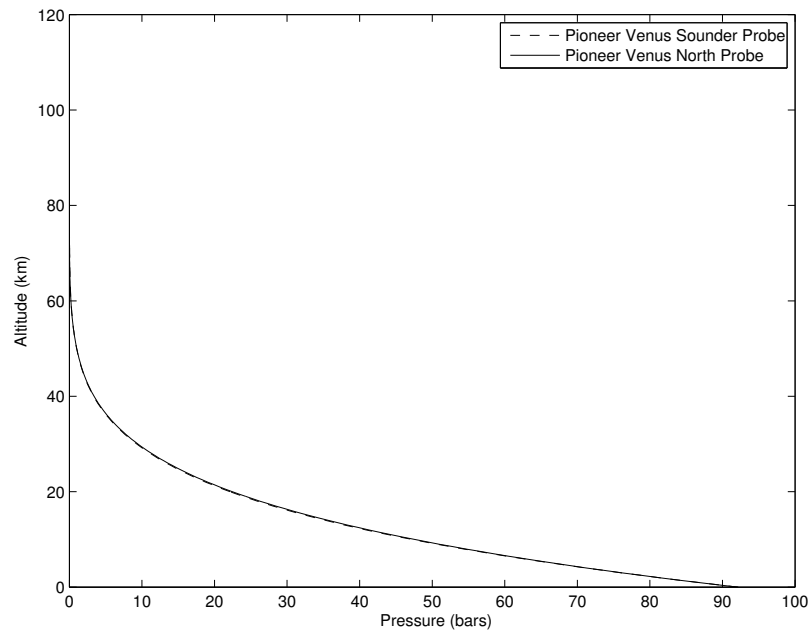


Figure 4.2: Pressure as a function of altitude in the Venus atmosphere obtained using the Pioneer-Venus sounder and north probes

N₂. The CO₂ and N₂ opacity formalism used in this RTM is

$$\alpha_{CO_2} = 1.12 \times 10^8 (q_{CO_2}^2 + 0.25 q_{CO_2} q_{N_2} + 0.0054 q_{N_2}^2) f^2 p^2 T^{-5} \quad (4.15)$$

where f is the frequency in GHz, p is the pressure in bars, T is the temperature in Kelvin, q is the number mole fraction, and α is the absorption in dB/km.

Gaseous SO₂

The second major opacity contribution comes from gaseous SO₂. In the developed RTM, the opacity formalism developed by Fahd and Steffes [12] is described below. The formalism developed by Fahd and Steffes was chosen over the Ben Reuven formalism by Sulieman et al. [37] due to its better performance when compared to laboratory measurements as shown previously in this work.

This formalism is based on the Van Vleck-Weisskopf formalism where the contribution from each rotational resonant line to the absorption at a particular frequency can be expressed as

$$\alpha = \alpha_{max} \left(\frac{f}{f_0} \right)^2 \gamma [((f_0 - f)^2 + \gamma^2)^{-1} + ((f_0 + f)^2 + \gamma^2)^{-1}] \quad (4.16)$$

where α_{max} is the absorption at the line centers, f is the frequency of interest, f_0 is the resonant line frequency, and γ is the line width. As per Fahd and Steffes [12] a line width of $\gamma_{SO_2/CO_2} = 5.25 \text{ GHz/bar}$ is used for the CO₂ broadening of SO₂ and a line width of $\gamma_{SO_2/SO_2} = 15 \text{ GHz/bar}$ is used for the self broadening of SO₂. Thus the formalism includes the effects of both CO₂ broadening and SO₂ self-broadening so that

$$\gamma = \gamma_{SO_2/CO_2} P_{CO_2} + \gamma_{SO_2/SO_2} P_{SO_2} \quad (4.17)$$

where P_{CO_2} and P_{SO_2} are the partial pressures (in bars) of gaseous CO₂ and SO₂ respectively.

Gaseous H_2SO_4

The next opacity contribution comes from gaseous H_2SO_4 . The formalism for the opacity of H_2SO_4 is based on a multiplicative expression fit to laboratory measurements done by Kolodner et al. 1997 [21]. There are six best fit expressions based on the frequency of the observation. The formalism is listed below

$$\alpha_{H_2SO_4}(f = 2.26) = 104.7 \times q_{H_2SO_4} P^{1.333} \left(\frac{553}{T} \right)^{3.2} \quad (4.18)$$

$$\alpha_{H_2SO_4}(f = 8.4) = 444.2 \times q_{H_2SO_4} P^{1.283} \left(\frac{553}{T} \right)^{3.0} \quad (4.19)$$

$$\alpha_{H_2SO_4}(f = 11.9) = 731.5 \times q_{H_2SO_4} P^{1.309} \left(\frac{553}{T} \right)^{2.9} \quad (4.20)$$

$$\alpha_{H_2SO_4}(f = 21.6) = 1945 \times q_{H_2SO_4} P^{1.08} \left(\frac{553}{T} \right)^{3.0} \quad (4.21)$$

$$\alpha_{H_2SO_4}(f < 12) = 33.25 \times q_{H_2SO_4} P^{1.333} f^{1.27} \left(\frac{553}{T} \right)^{3.0} \quad (4.22)$$

$$\alpha_{H_2SO_4}(f) = 54.9 \times q_{H_2SO_4} P^{1.333} f^{1.15} \left(\frac{553}{T} \right)^{3.0} \quad (4.23)$$

where f is the frequency, $q_{H_2SO_4}$ is the mixing ratio of gaseous H_2SO_4 , P is the pressure in bars, and T is the temperature in Kelvin. This RTM implements all of the previously listed formalisms based on the appropriate frequency.

Liquid H_2SO_4

The formalism for the opacity of clouds is taken from Fahd [11] and is

$$\alpha_{cloud} = \frac{246M\epsilon_r''}{\rho\lambda[(\epsilon_r' + 2)^2 + (\epsilon_r'')^2]} \quad (4.24)$$

where ρ is the density of the liquid sulfuric acid ($1.84E9 \text{ mg/m}^3$), M is the bulk density of the cloud (50 mg/m^3), λ is the wavelength in km and ϵ_r' and ϵ_r'' are the real and imaginary parts of the complex dielectric constant of the liquid which is found using

$$\epsilon_r = 3.3 + \frac{84.2}{(1 + (2\pi f(1.7 \times 10^{-11}))^{0.91})} \quad (4.25)$$

with f is the frequency in Hz. Since clouds are only formed between 48-50 km the absorption is only appropriate for the temperatures associated with that range of altitudes.

4.2.3 Abundance Profiles

The principal constituent of the Venus atmosphere is gaseous CO_2 which comprises 96.5% of the atmosphere. Gaseous N_2 constitutes about 3.5% of the atmosphere. In this RTM these mole fractions are used for all altitudes of the Venus atmosphere.

For gaseous H_2SO_4 , the developed RTM implements a saturation vapor pressure model as done in Kolodner [21]. This model is based on Mariner 10 radio occultation experiments observed by Lipa and Tyler [24]. For altitudes less than 48 km it is assumed that the H_2SO_4 mixing ratio is zero. For altitudes above 48 km the partial pressure of H_2SO_4 is

$$P_{H_2SO_4} = 1.01325 \exp \left(10156 \left[-\frac{1}{T} + \frac{0.38}{T_c - T_o} \left(1 + \ln \frac{T_o}{T} - \frac{T_o}{T} \right) \right] - \frac{\Delta F}{RT} + 16.259 \right) \quad (4.26)$$

where $P_{H_2SO_4}$ is the partial pressure of H_2SO_4 (in bars), T is the temperature in Kelvin, T_c is the critical temperature of 910.5 K, T_o is the reference temperature of 375 K, ΔF is change in chemical potentials (477.60 J/mole) [13], and R is the ideal gas constant (8.3143 J/mole-K). Different abundance profiles can be used in place of this simple one.

Finally a variable abundance profile for gaseous SO_2 is implemented in the developed RTM. A uniform mixing ratio of any value can be selected for altitudes below the main cloud layer (i.e. < 48 km). Above the cloud layer the SO_2 abundance profile is assumed to decay exponentially with a scale height of 3.3 km [28]. This is calculated by the following

$$q_{SO_2}(z) = \begin{cases} SO_{2_{surf}} & : z < 48 \\ SO_{2_{surf}} \times \exp(-(z - 48)/3.3); & : z \geq 48 \end{cases} \quad (4.27)$$

where $SO_{2_{surf}}$ is the variable mixing ratio of SO_2 at the surface and z is the location of the current altitude layer.

4.2.4 Index of Refraction

The refractive index is important in calculating the path that a ray takes through the atmosphere. Given the known concentration of CO_2 and N_2 as well as the density-normalized refractivity values, the refractivity profile $N(z)$ is computed via

$$N(z) = \frac{NP(z)}{RT(z)} \quad (4.28)$$

where $P(z)$ is the pressure, $T(z)$ is the temperature, R is the ideal gas constant, and N is the normalized refractivity of a 95.5% CO_2 3.5% N_2 atmosphere ($251.09m^3/kg$) [10]. The refractive index profile $n(z)$ is defined in terms of refractivity via

$$n(z) = N(z) \times 10^{-6} + 1 \quad (4.29)$$

4.3 Ray-tracing

While a basic radiative transfer equation can be used to solve for brightness temperatures measured by an orbiting spacecraft, the basic formalism assumes an infinitely narrow beamwidth. The formalism also neglects the effects of refraction between atmospheric layers. Here we present a more advanced ray tracing approach used in the developed RTM employing the technique described by Hoffman [18].

4.3.1 Ray-tracing Described

Most radio observations of planets are done by measuring emitted rays originating deep in the atmosphere. However, for modeling purposes it is easier to model ray-paths originating from the observer and entering the planet's atmosphere. These are equivalent by reciprocity.

The origin of the ray is the location of the radiometer (either on the spacecraft or on earth) in a Cartesian space with the origin defined as the center of the planet.

Reference figure 4.3 for the following discussion. The initial ray direction is set as the pointing direction of the antenna. First the boresight ray-path is calculated. Once the ray intersects the first layer, the vector location of this intersection is recorded. From this, the local normal (ray pointing from the origin to the location of intersection) and the zenith angle can be calculated. The incidence angle is found and Snell's law is applied to find the vector direction of the transmitted ray. Once the vector direction is determined, the vector origin of the ray-segment is set as the initial intersection. A new sphere is defined by the next layer and the ray-sphere intersection algorithm is applied with the new inputs. The algorithm calculates the distance and this is recorded. Using this distance, the new intersection is calculated (which can be either at the next deeper layer or the previous layer). The latter occurs only when observing the limb of the planet. This continues until the ray hits the planetary surface, exits from the back of the planet, or becomes so opaque that no significant transmission occurs.

When the ray hits the planetary surface, the incidence angle is recorded and is used to find the emissivity of the planet (Equations 4.12, 4.13). If the ray does not hit the surface of the planet, the incidence angle is not recorded and no surface temperature is calculated. The ray has a possibility of orbiting the planet; this occurs if the next layer causes critical refraction. When this occurs, the layers pathlength is set to infinity which sets the brightness temperature of the layer to its thermal temperature. The emission from this layer is then attenuated by the layers above.

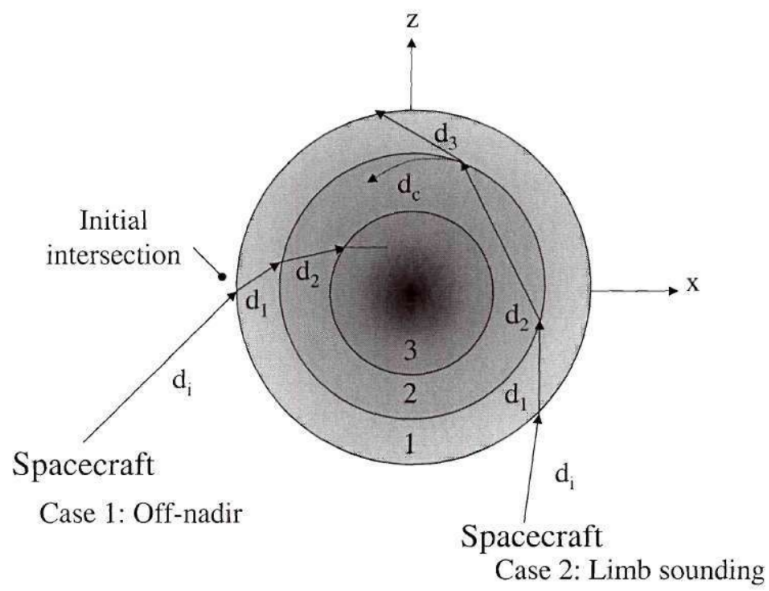


Figure 4.3: A two dimensional graphic example of the ray-tracing process taken from Hoffman 2001 [18]. An off-nadir (left) and a limb sounding case (right) are shown. Two possible outcomes for the limb-sounding case are shown. d_3 shows the ray exiting the atmosphere, while d_c shows critical refraction.

4.3.2 Ray-tracing Algorithm Mathematics

The mathematical foundation for the ray-tracing component of the RTM is developed in this section. The ray-sphere intersection algorithm begins with definition of the parametric equation for a ray. A ray is defined as,

$$\begin{aligned} R_{origin} &= R_o = \begin{bmatrix} X_o & Y_o & Z_o \end{bmatrix} \\ R_{direction} &= R_d = \begin{bmatrix} X_d & Y_d & Z_d \end{bmatrix} \end{aligned} \quad (4.30)$$

where

$$\|R_d\|_2^2 = 1 \quad (4.31)$$

which defines a ray as a set of points described by the equation for a line

$$R = R_o + R_d \times t \quad (4.32)$$

where time, t is greater than zero. The sphere is defined by,

$$\begin{aligned} S_{center} &= S_c = \begin{bmatrix} X_c & Y_c & Z_c \end{bmatrix} \\ S_{radius} &= S_r \\ S_{surface} &= S_s = \begin{bmatrix} X_s & Y_s & Z_s \end{bmatrix} \end{aligned} \quad (4.33)$$

where

$$\|S_s - S_c\|_2^2 = S_r^2 \quad (4.34)$$

Using equation 4.32 as the intersection equation for the ray we can substitute that into equation 4.34, resulting in,

$$\|(R_o + R_d \times t) - S_c\|_2^2 = S_r^2 \quad (4.35)$$

which can be expanded to

$$(X_o + X_d t - X_c)^2 + (Y_o + Y_d t - Y_c)^2 + (Z_o + Z_d t - Z_c)^2 = S_r^2 \quad (4.36)$$

This can be simplified into a quadratic equation

$$At^2 + Bt + C = 0 \quad (4.37)$$

where,

$$A = \|R_d\|_2^2 = 1 \quad (4.38)$$

$$B = 2((R_o - S_c) \bullet R_d) \quad (4.39)$$

$$C = \|R_o - S_c\|_2^2 - S_r^2 \quad (4.40)$$

The solutions to this equation are the standard quadratic solutions

$$t_{0,1} = \frac{-B \pm \sqrt{B^2 - 4AC}}{2A} \quad (4.41)$$

where the t 's (solutions) are the distance to the intersection point from the ray origin. If the discriminant of these equations is negative the ray misses the sphere. For the purpose of the RTM these are the cases where the ray misses the planet or it exits out of the planet's atmosphere. The smallest positive t value is the correct solution. Once the t is found the vector location of the intersection is

$$r_{int} = r_i = \begin{bmatrix} x_i & y_i & z_i \end{bmatrix} = \begin{bmatrix} X_o + X_d t & Y_o + Y_d t & Z_o + Z_d t \end{bmatrix} \quad (4.42)$$

and the unit vector normal at the surface is then

$$r_{normal} = r_n = \frac{(r_i - S_c)}{S_r} = \begin{bmatrix} \frac{(x_i - X_c)}{S_r} & \frac{(y_i - Y_c)}{S_r} & \frac{(z_i - Z_c)}{S_r} \end{bmatrix} \quad (4.43)$$

In terms of the RTM, the solution to the quadratic equation (t) is the distance the ray travels through a given layer. The origin of the transmitted ray is set at the intersection location r_{int} and the direction of the transmitted ray is calculated from the intersection r_{int} and the surface normal r_{normal} using Snell's law.

The vector form of Snell's law requires two vectors: the incident ray vector (\mathbf{I}) and the local surface normal (\mathbf{N}). Refer to Figure 4.4 for a graphical demonstration. The incident angle is calculated using

$$\cos(\theta_1) = -\mathbf{I} \bullet \mathbf{N} \quad (4.44)$$

From Snell's law, the relative index of refraction (η) is,

$$\eta = \frac{\sin(\theta_2)}{\sin(\theta_1)} = \frac{\eta_1}{\eta_2} \quad (4.45)$$

The angle of the transmitted ray (θ_2) can be computed from known quantities,

$$\cos(\theta_2) = \sqrt{(1 - \sin^2(\theta_2))} = \sqrt{(1 - \eta^2 \sin^2(\theta_1))} = \sqrt{(1 - \eta^2(1 - \cos^2(\theta_1)))} \quad (4.46)$$

The vector direction of the transmitted ray is computed as,

$$\mathbf{T} = \eta \mathbf{I} + (\eta \cos(\theta_1) - \cos(\theta_2)) \mathbf{N} \quad (4.47)$$

the values of \mathbf{I} and \mathbf{N} are the vectors R_d and r_n respectively. The output of this formula (\mathbf{T}) is the new value for R_d . Using this algorithm and techniques described in the previous sections we can trace a path through each layer of the atmosphere.

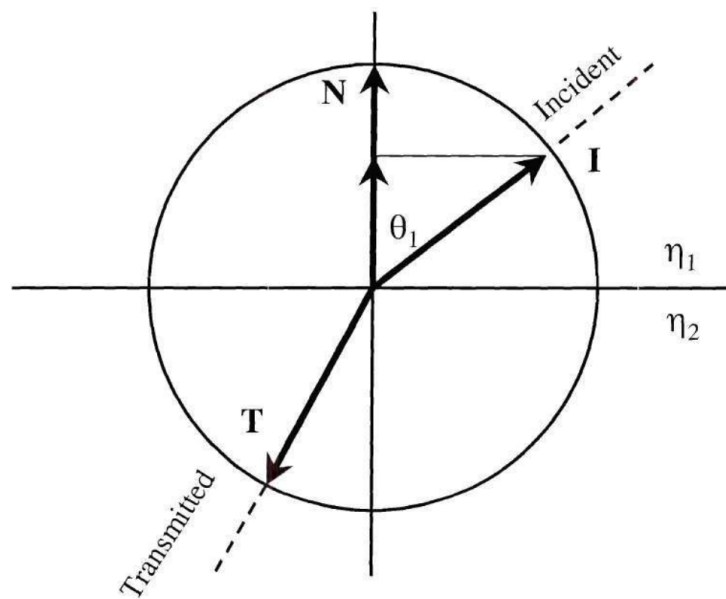


Figure 4.4: Vector implementation of Snell's Law. Image courtesy of Hoffman 2001 [18]

4.4 Vector Radiative Transfer

A typical method of radiative transfer modeling is to iterate through each layer and calculate the layer's RTM parameters and temperature. While computing an RTM this way is easier to understand, it is extremely inefficient. The following section describes a more efficient way of computing a radiative transfer model.

4.4.1 Thermo-Chemical Model (TCM)

The first step of a vector radiative transfer model is to compute the TCM for the Venus atmosphere. The TCM is dependent on the altitude vector \mathbf{a} whose size is $N \times 1$ where N is the number of layers in the altitude. \mathbf{a} is defined as

$$a_i = iz_{step} \quad (4.48)$$

where a_i is the i^{th} element in the vector and z_{step} is the distance between each atmospheric layer.

The TCM for Venus requires a latitude of observation. This is due to the latitudinal variations of the temperature-pressure profiles of the planet. Using the altitude vector, \mathbf{a} , it is possible to calculate the T-P profiles of the atmospheric layers of interest using a one dimension interpolation of the T-P profiles as reported by the Pioneer-Venus sounder and north probes. The temperature and pressure vectors are \mathbf{T} and \mathbf{P} respectively. Using the \mathbf{T} and \mathbf{P} , it will be possible to create a vector for all constituents mixing ratio \mathbf{Q}_c , with c being the constituent of interest. The refractive index vector \mathbf{N} can be calculated using the same methods as \mathbf{Q}_c . The vectors \mathbf{T} , \mathbf{P} , \mathbf{Q}_c , and \mathbf{N} are of size $N \times 1$.

4.4.2 Absorption Matrix

The absorption matrix \mathbf{A} needs to be calculated. This is done by

$$A_{i,f} = \sum_{constituents} \alpha_{i,c}(\mathbf{F}(f)) \quad (4.49)$$

where A_i is the i^{th} element in the vector and $\alpha_{i,c}(f)$ is the absorption of the constituent c at the i^{th} layer in the atmosphere and \mathbf{F} is the vector of all frequencies which is $1 \times M$ with M being the number of frequencies. \mathbf{A} is of size $N \times M$.

4.4.3 Ray-Tracing

In this method, Ray-Tracing is still done iteratively, but in this case we start with a distance vector \mathbf{d} of size $N \times 1$ such that all elements in the vector are zero,

$$\mathbf{d} = \vec{0}$$

and for every t (the distance the ray traveled in a layer) calculated in the Ray-tracing algorithm the vector \mathbf{d} is updated using

$$\mathbf{d}_i = \mathbf{d}_i + t \quad (4.50)$$

This keeps track of the total distance spent in each layer.

4.4.4 Radiative Transfer Model

Several variables are calculated in this RTM. The first is the opacity matrix, $\vec{\tau}$, which is defined as

$$\tau_{i,j} = \alpha_{i,j} \times \mathbf{d}_i \quad (4.51)$$

where α is the opacity at layer i at frequency j , and \mathbf{d} is the distance the ray travels through layer i

Using the opacity matrix it is possible to calculate the weighting matrix for the upwelling and downwelling of the atmosphere, \mathbf{W}_{up} and \mathbf{W}_{down} respectively, using the following

$$\mathbf{W}_{up,i,j} = (1 - e^{-\tau_{i,j}})e^{(-\sum_{l=i+1}^N \tau_{l,j})} \quad (4.52)$$

$$\mathbf{W}_{down,i,j} = (1 - e^{-\tau_{i,j}})e^{(-\sum_{l=1}^{i-1} \tau_{l,j})}e^{(-\sum_{l=1}^N \tau_{l,j})}(1 - \epsilon(\theta)) \quad (4.53)$$

where i is again each layer of the atmosphere, j is each frequency of interest and $\epsilon(\theta)$ is the surface emissivity. \mathbf{W}_{up} calculates the attenuation of the current layer and

every layer above it. \mathbf{W}_{down} calculates the attenuation from the current layer towards the surface and back through the entire atmosphere.

These weighting vectors along with the temperature vector, \mathbf{T} , gives the expected temperature brightness through

$$\begin{aligned} \mathbf{Tb}_j = & T_{surf} \cdot \epsilon(\theta) \cdot e^{(-\sum_{l=1}^N \tau_{l,j})} + T_{cmb} \cdot (1 - \epsilon(\theta)) \cdot e^{(-2\sum_{l=1}^N \tau_{l,j})} \\ & + \sum_{i=1}^N \mathbf{T}_i \cdot \mathbf{W}_{up_{i,j}} + \sum_{i=1}^N \mathbf{T}_i \cdot \mathbf{W}_{down_{i,j}} \end{aligned} \quad (4.54)$$

where the first term is the temperature at the surface multiplied by the emissivity and attenuated by the atmosphere. The second term is the cosmic microwave background (2.7K) multiplied by the reflectivity of the planet then attenuated by the atmosphere twice (down and back up). The third term is the upwelling of the atmosphere which is the temperature at each level multiplied by the upwelling weighting matrix described previously. The final term is the downwelling of the atmosphere which again is the temperature at each level multiplied by the downwelling weighting matrix defined previously.

4.5 *Beam Forming*

Since the ray-tracing algorithm assumes a pencil beam (or ray) it is necessary to form spatial samples of the main beam of an antenna in order to properly estimate the emergent flux of the atmosphere incident on the antenna. This is accomplished by generating a set of vectors that each describe a ray that is offset from the direction of the boresight ray. Since the developed RTM is used for earth based observations the problem of mapping an antenna to the planet gets simplified. The parameters of this beam forming algorithm are R_{proj} , $BWHM$, N_c , and n_0 . R_{proj} is the projected radius of the antenna beam pattern onto a planar projection of Venus (in km). This results an equivalent pixel resolution (1 pixel = 200x200 km). The second parameter is the 3dB beamwidth of the antenna's main beam. N_c is the number of concentric

rings while n_0 is the number of samples in the initial ring. Once the free samples are chosen the number of beamsamples in each ring may be found by

$$N(k) = (2k - 1) \quad (4.55)$$

where N is the number of samples and k is the integer multiple of the ring spacing in terms of radius. For example, if a ring spacing of $1/3$ of the half-power beamwidth is chosen, then there will be three concentric rings sampling the beam ($N_c = 3$). Thus if the first ring is sampled at 90° , there will be four beamsamples in the first ring ($360^\circ/n_0 = 90^\circ$ for $n_0 = 4$). $\Delta\phi$ is defined as the current spacing between each beamsample in the current ring and can be found by

$$\Delta\phi(k) = \frac{BWHM}{k}. \quad (4.56)$$

Using $\Delta\phi$ allows for us to calculate the weight of each beamsample using

$$beamweight(\Delta\phi) = e^{\left(-2.76 \times \left(\frac{\Delta\phi}{BWHM}\right)^2\right)} \quad (4.57)$$

Combining equation 4.56 and 4.57 it is possible to remove the need for $BWHM$.

$$beamweight(k) = e^{\left(-2.76 \times \left(\frac{1}{k}\right)^2\right)} \quad (4.58)$$

The spatial resolution of the beamsampling may be increased and is limited by only the memory of the computer and the patience of the user.

4.6 Radiative Transfer Results

To validate the developed RTM, results from disk-averaged computations were compared to various disk-averaged brightness measurements taken of Venus. Table 2 shows results for measurements of the microwave and millimeter-wave disk-averaged brightness temperatures of Venus. For comparison purposes the table also shows the computed disk-averaged brightness temperatures (T_D) for Venus using the developed RTM.

For the lower frequencies our computed T_D is much higher than the measured values. This is likely due to the relatively simple model used for surface emissivity. The larger values computed at higher frequencies are likely due to the value assumed for $SO_{2_{surf}}$, (75 ppm) and could be adjusted by changing that value.

Figure 4.5 shows the weighting function of various frequencies. Changing the SO_2 and H_2SO_4 abundance profiles will result in a change in the weighting functions as well as the disk-averaged temperature.

Table 2: Measured Disk-Averaged Brightness Temperatures of Venus for Various Frequencies as compared to the results from the new Radiative Transfer Model

Frequency (GHz)	Wavelength (cm)	Measured T_D (K)	Computed T_D (K)	Reference of Measurements
1.385	21.66	612.8 ± 12.3	642.6	Butler et al., 2001 [3]
1.42	21.12	617 ± 25	642.7	Berge et al., 1972 [2]
1.5	20.00	636 ± 28	643.1	Pettengill et al., 1988 [29]
2.91	10.31	620 ± 30	651.4	Vetukhnovskaya et al., 1969 [39]
4.86	6.41	679.9 ± 13.6	654.1	Butler et al., 2001 [3]
5.0	6.0	652 ± 30	653.7	Berge et al., 1972 [2]
8.42	3.56	652 ± 15	621.3	Steffes et al., 1990 [34]
8.44	3.55	657.5 ± 13.2	621.0	Butler et al., 2001 [3]
9.62	3.12	608 ± 35	605.4	Berge et al., 1972 [2]
11.11	2.70	612 ± 37	585.9	McCullough et al., 1972 [26]
13.3	2.26	561 ± 19	559.3	Steffes et al., 1990 [34]
14.94	2.00	565.8 ± 17	542.1	Suleiman et al., 1997 [36]
14.94	2.00	565.9 ± 17	542.1	Butler et al., 2001 [3]
18.46	1.63	520 ± 17	511.2	Steffes et al., 1990 [34]
22.25	1.35	507 ± 22	485.0	Steffes et al., 1990 [34]
22.46	1.34	505.2 ± 25.3	483.7	Butler et al., 2001 [3]
22.46	1.34	499.1 ± 25	483.7	Suleiman et al., 1997 [36]
37.50	0.80	440 ± 35	421.6	Vetukhnovskaya et al., 1969 [39]
86.1	0.35	357.5 ± 13.1	345.7	Ulich et al., 1980 [38]

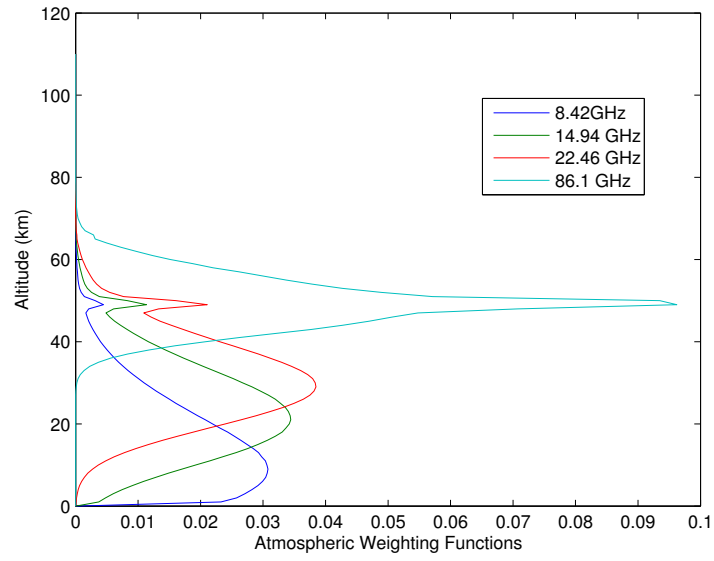


Figure 4.5: Disk-averaged weighting function of the Venus atmosphere at frequencies of 8.42, 14.94, 22.46, and 86.1 GHz.

CHAPTER V

SUMMARY AND CONCLUSIONS

The objective of this Thesis has been to advance the understanding of the millimeter-wavelength properties of gaseous sulfur dioxide under Venus conditions. Extensive laboratory measurements of the 2-4 mm-wavelength properties of sulfur dioxide under simulated upper troposphere conditions of Venus were conducted. These along with previous laboratory measurements (Fahd and Steffes [12], Suleiman et al. [37], and Steffes et al. [35]) have been used to validate absorption formalisms. A discussion of the significance of these results and future work are presented below.

With the approaching completion of the ESA Venus Express Mission, Earth-based centimeter and millimeter-wavelength observations of Venus are becoming more important. Knowledge of the absorption properties of sulfur dioxide will be important in analyzing data from these earth-based observations.

5.1 Significant Results

Laboratory measurements taken of the millimeter-wavelength absorption of sulfur dioxide under Venus conditions has verified the formalism for sulfur dioxide opacity developed by Fahd and Steffes [12]. The model is able to fit 85.88% of the laboratory data (centimeter-wavelength done by Steffes et al. 2014 [35], millimeter-wavelength presented in this work) within 2σ uncertainty. The bounds verified by laboratory data are set to frequencies between 1-150 GHz, temperatures between 307-550 K, and concentrations between 0-100% of SO₂/volume.

5.2 *Application to Venus Observations*

Verifying that the Fahd and Steffes [12] model correctly predicted the absorption of SO_2 at centimeter and millimeter-wavelengths allows for analysis of earth-based observations from radio telescopes. Verifying the model has allowed for the development of a Radiative Transfer Model (RTM) which can successfully simulate and predict expected observations of Venus.

One such radio telescope is the Combined Array for Research in Millimeter-wave Astronomy (CARMA). Observations of Venus using CARMA have been recently completed by Devaraj [7] at frequencies ranging from 98-115 GHz. Using these maps, along with the RTM developed, maps of the variations observed can be produced. Variation in these maps can be used to identify anomalies in Venus's atmosphere such as storms or potential volcanic eruptions.

Along with CARMA, other observations of Venus have been made. One such observation was done by Sagawa [32]. Sagawa mentions it is possible to extract abundance profiles for both SO_2 and H_2SO_4 from observations done at two different frequencies. This requires knowledge of the frequency dependence of the absorption from both gasses. While this work characterizes the absorption of SO_2 , work is still needed to characterize the absorption spectrum of H_2SO_4 in the millimeter-wavelength regime.

Sub-millimeter-wavelength observations were done with ALMA (Atacama Large Millimeter Array) in 2011 [27]. These observations were the first high-resolution map of the day hemisphere at millimeter-wavelengths. They showed how the mesosphere was affected by solar-winds, the mesospheric water distribution, and the moderate equatorial zonal winds. Using this data along with the developed RTM and methods described in Sagawa [32], it is possible to retrieve an abundance profile for multiple constituents of Venus' upper atmosphere.

5.3 Suggestions for Future Work

Many improvements can be made to the newly-developed RTM. The biggest is an accurate formalism for the millimeter-wavelength absorption of gaseous H_2SO_4 . The formalism used in the current model was developed from centimeter-wavelength data. A new laboratory measurement system to better characterize gaseous H_2SO_4 's millimeter-wavelength absorption spectrum is being developed at Georgia Institute of Technology's Planetary Atmospheres Lab. These measurements, along with those from Kolodner et al. [22] should help develop a formalism for the gaseous H_2SO_4 absorption spectra at centimeter and millimeter-wavelengths.

The development of a Radiative Transfer Model is the first step in creating an ability to retrieve constituent abundances in the Venus atmosphere. Creation of such model will allow for retrieval of abundance profiles and temperature-pressure profiles from observations of the planet. A centimeter wavelengths retrieval algorithms has already been developed for gaseous H_2SO_4 and temperature (Jenkins et al. [19]). These results will carry such work into the millimeter-wave spectrum.

APPENDIX A

REFRACTIVITY OF SO₂

Table 3 shows the normalized refractivity of SO₂ calculated from the data in this thesis. Methods used to calculate the refractivity and the appropriate 2σ are taken from Hanley 2008 [14]

Table 3: Normalized refractivity of SO₂ in a CO₂ atmosphere.

Temperature (K)	Total Pressure (bar)	Frequency (GHz)	q _{SO₂} (%)	N _{ρ_{SO₂}} × 10 ⁻¹⁶	2σ error × 10 ⁻¹⁶
308.75	0.03	103.09	84.7	1.65	0.350
308.75	0.03	110.37	84.7	1.50	0.320
308.75	0.03	118.44	84.7	1.62	0.340
308.75	0.03	122.48	84.7	1.65	0.350
308.55	0.970	103.04	2.62	3.87	0.810
308.55	0.970	110.30	2.62	3.84	0.8
308.55	0.970	118.38	2.62	3.89	0.820
308.55	0.970	122.42	2.62	3.92	0.820
308.65	2	102.97	1.27	7	1.45
308.65	2	110.24	1.27	6.97	1.44
308.65	2	115.08	1.27	7.12	1.48
308.65	2	118.30	1.27	6.99	1.45
308.65	2	122.34	1.27	7.05	1.46
307.55	0.120	79.590	84.7	1.70	0.1

307.55	0.120	83.620	84.7	1.71	0.1
307.55	0.120	93.510	84.7	1.72	0.1
307.55	0.120	98.350	84.7	1.75	0.1
307.55	0.120	102.39	84.7	1.80	0.110
307.55	0.120	110.26	84.7	1.73	0.1
307.25	0.940	79.550	10.420	2.04	0.130
307.25	0.940	83.590	10.420	2.05	0.130
307.25	0.940	93.470	10.420	2.06	0.130
307.25	0.940	98.310	10.420	2.08	0.140
307.25	0.940	102.34	10.420	2.09	0.140
307.25	1.99	79.510	4.94	2.64	0.180
307.25	1.99	83.540	4.94	2.64	0.180
307.25	1.99	93.420	4.94	2.64	0.180
307.25	1.99	98.250	4.94	2.66	0.180
307.25	1.99	102.28	4.94	2.67	0.180
307.25	1.99	110.14	4.94	2.69	0.180
344.45	0.09	1.64	84.7	1.61	0.120
344.45	0.09	103.06	84.7	1.67	0.130
344.45	0.09	110.33	84.7	1.62	0.130
344.45	0.09	115.17	84.7	1.66	0.130
344.45	0.09	118.40	84.7	1.63	0.120
344.45	0.09	122.44	84.7	1.70	0.130
344.45	0.09	124.86	84.7	1.74	0.130
344.45	0.09	127.28	84.7	1.82	0.150
344.45	0.09	137.60	84.7	1.64	0.140
344.65	0.920	1.59	8.26	2.66	0.210
344.65	0.920	103.01	8.26	2.64	0.210

344.65	0.920	110.27	8.26	2.65	0.210
344.65	0.920	115.12	8.26	2.68	0.210
344.65	0.920	118.35	8.26	2.69	0.210
344.65	0.920	122.38	8.26	2.69	0.210
344.65	0.920	124.80	8.26	2.77	0.220
344.65	0.920	127.22	8.26	2.79	0.240
344.65	0.920	137.53	8.26	2.68	0.250
343.95	1.97	1.53	3.88	3.94	0.4
343.95	1.97	102.95	3.88	3.95	0.310
343.95	1.97	110.21	3.88	3.92	0.310
343.95	1.97	115.05	3.88	3.98	0.320
343.95	1.97	118.27	3.88	3.97	0.310
343.95	1.97	122.31	3.88	3.98	0.310
343.95	1.97	124.73	3.88	3.95	0.330
343.95	1.97	127.16	3.88	3.38	0.310
343.95	1.97	137.45	3.88	3.94	0.360
344.35	0.03	1.66	84.7	1.25	0.250
344.35	0.03	103.08	84.7	1.34	0.260
344.35	0.03	110.35	84.7	1.23	0.250
344.35	0.03	115.20	84.7	1.34	0.270
344.35	0.03	118.43	84.7	1.30	0.260
344.35	0.03	122.47	84.7	1.33	0.260
344.35	0.03	127.31	84.7	1.54	0.310
344.35	0.03	137.62	84.7	1.21	0.290
344.55	0.940	1.61	2.96	2.35	0.490
344.55	0.940	103.03	2.96	4.03	0.760
344.55	0.940	110.29	2.96	4.09	0.780

344.55	0.940	115.14	2.96	4.09	0.780
344.55	0.940	118.37	2.96	4.11	0.780
344.55	0.940	122.40	2.96	4.12	0.780
344.55	0.940	124.82	2.96	4.18	0.8
344.55	0.940	127.25	2.96	4.28	0.940
344.55	0.940	137.55	2.96	3.98	0.880
344.45	2.01	1.54	1.39	7.99	2.64
344.45	2.01	102.96	1.39	7.63	1.43
344.45	2.01	110.22	1.39	7.60	1.43
344.45	2.01	115.07	1.39	7.61	1.43
344.45	2.01	118.29	1.39	7.67	1.44
344.45	2.01	122.33	1.39	7.67	1.44
344.45	2.01	124.75	1.39	7.65	1.44
344.45	2.01	137.47	1.39	7.62	1.55
343.65	0.1	79.620	84.7	1.72	0.110
343.65	0.1	83.650	84.7	1.73	0.120
343.65	0.1	85.470	84.7	1.68	0.120
343.65	0.1	90.320	84.7	1.38	0.290
343.65	0.1	102.22	84.7	1.79	0.120
343.65	0.1	110.30	84.7	1.74	0.120
343.25	0.940	79.580	9.14	2.34	0.170
343.25	0.940	83.620	9.14	2.35	0.170
343.25	0.940	85.440	9.14	2.33	0.170
342.95	2.02	79.530	4.24	3.33	0.240
342.95	2.02	83.570	4.24	3.33	0.240
342.95	2.02	85.390	4.24	3.30	0.250
343.15	0.06	79.630	84.7	1.48	0.160

343.15	0.06	83.670	84.7	1.49	0.170
343.15	0.06	90.340	84.7	1.51	0.160
343.15	0.06	102.24	84.7	1.59	0.170
343.15	0.06	110.32	84.7	1.51	0.160
343.65	0.930	79.6	5.48	2.82	0.310
343.65	0.930	83.630	5.48	2.84	0.310
343.65	0.930	110.27	5.48	2.89	0.320
343.95	2	79.550	2.54	4.50	0.5
343.95	2	83.580	2.54	4.51	0.5

REFERENCES

- [1] BARRETT, A. H., “Microwave absorption and emission in the atmosphere of venus,” *Journal of Geophysical Research*, vol. 65, no. 6, pp. 1835–1838, 1960.
- [2] BERGE, G., MUHLEMAN, D., and ORTON, G., “High resolution interferometric observations of venus at three radio wavelengths,” *Icarus*, vol. 17, no. 3, pp. 675 – 681, 1972.
- [3] BUTLER, B. J., STEFFES, P. G., SULEIMAN, S. H., KOLODNER, M. A., and JENKINS, J. M., “Accurate and consistent microwave observations of venus and their implications,” *Icarus*, vol. 154, no. 2, pp. 226 – 238, 2001.
- [4] DEBOER, D. R. and STEFFES, P. G., “Laboratory Measurements of the Microwave Properties of H₂S under Simulated Jovian Conditions with an Application to Neptune,” *Icarus*, vol. 109, pp. 352–366, November 1993.
- [5] DEBOER, D. R. and STEFFES, P. G., “Laboratory measurements of the microwave properties of {H₂S} under simulated jovian conditions with an application to neptune,” *Icarus*, vol. 109, no. 2, pp. 352 – 366, 1994.
- [6] DEVARAJ, K., *The Centimeter- and Millimeter-Wavelength Ammonia Absorption Spectra Under Jovian Conditions*. PhD thesis, Georgia Institute of Technology, December 2011.
- [7] DEVARAJ, K. private communication, 2014.
- [8] DEVARAJ, K. and STEFFES, P. G., “The Georgia Tech millimeter-wavelength measurement system and some applications to the study of planetary atmospheres,” *Radio Science*, vol. 46, no. 2, 2011.
- [9] ESPOSITO, L. W., “Planetary science: Rising sulphur on Venus,” *Nature Geoscience*, vol. 6, no. 1, pp. 20 – 21, 2012.
- [10] ESSEN, L. and FROOME, K. D., “The refractive indices and dielectric constants of air and its principal constituents at 24,000 mc/s,” *Proceedings of the Physical Society. Section B*, vol. 64, no. 10, p. 862, 1951.
- [11] FAHD, A. K., *Study and Interpretation of the Millimeter-wave Spectrum of Venus*. PhD thesis, Georgia Institute of Technology, June 1992.
- [12] FAHD, A. K. and STEFFES, P. G., “Laboratory measurements of the microwave and millimeter-wave opacity of gaseous sulfur dioxide (SO₂) under simulated conditions for the Venus atmosphere,” *Icarus*, vol. 97, no. 2, pp. 200–210, 1991.

- [13] GIAUQUE, W. F., HORNUNG, E. W., KUNZLER, J. E., and RUBIN, T. R., “The thermodynamic properties of aqueous sulfuric acid solutions and hydrates from 15 to 300k.1,” *Journal of the American Chemical Society*, vol. 82, no. 1, pp. 62–70, 1960.
- [14] HANLEY, T., *The Microwave Opacity Effects of Ammonia and Water Vapor Application to Remote Sensing of the Atmosphere of Jupiter*. PhD thesis, Georgia Institute of Technology, August 2008.
- [15] HANLEY, T. R. and STEFFES, P. G., “A high-sensitivity laboratory system for measuring the microwave properties of gases under simulated conditions for planetary atmospheres,” *Radio Science*, vol. 42, no. 6, 2007.
- [16] Hewlett-Packard, Santa Rosa, CA, *HP 8560 E-Series Spectrum Analyzer Calibration Guide*, 1997.
- [17] HO, W., KAUFMAN, I. A., and THADDEUS, P., “Laboratory measurement of microwave absorption in models of the atmosphere of venus,” *Journal of Geophysical Research*, vol. 71, no. 21, pp. 5091–5108, 1966.
- [18] HOFFMAN, J. P., *Microwave Opacity of Phosphine: Application to Remote Sensing of the Atmospheres of the Outer Planets*. PhD thesis, Georgia Institute of Technology, April 2001.
- [19] JENKINS, J. M., KOLODNER, M. A., BUTLER, B. J., SULEIMAN, S. H., and STEFFES, P. G., “Microwave remote sensing of the temperature and distribution of sulfur compounds in the lower atmosphere of venus,” *Icarus*, vol. 158, no. 2, pp. 312 – 328, 2002.
- [20] KARPOWICZ, B. M., *In search of water vapor on Jupiter: laboratory measurements of the microwave properties of water vapor and simulations of Jupiter’s microwave emission in support of the Juno mission*. PhD thesis, Karpowicz, 2010.
- [21] KOLODNER, M. A., *Microwave Remote Sensing of Sulfuric Acid Vapor in the Venus Atmosphere*. PhD thesis, Georgia Institute of Technology, June 1997.
- [22] KOLODNER, M. A. and STEFFES, P. G., “The microwave absorption and abundance of sulfuric acid vapor in the venus atmosphere based on new laboratory measurements,” *Icarus*, vol. 132, no. 1, pp. 151 – 169, 1998.
- [23] LIOU, K., *An Introduction to Atmospheric Radiation*. San Diego, California: Academic Press, 2002.
- [24] LIPA, B. and TYLER, G. L., “Statistical and computational uncertainties in atmospheric profiles from radio occultation: Mariner 10 at venus,” *Icarus*, vol. 39, no. 2, pp. 192 – 208, 1979.

- [25] MATTHAEI, G. L. and JONES, E., *Microwave filters, impedance matching networks and coupling structures*. New York: McGraw-Hill, 1980.
- [26] MCCULLOUGH, T., "Phase dependence of the 2.7 cm wavelength radiation of venus," *Icarus*, vol. 16, no. 2, pp. 310 – 313, 1972.
- [27] MORENO, R., MOULLET, A., ENCRENAZ, T., LELLOUCH, E., and FOUCHET, T., "Submillimeter spectroscopy of venus atmosphere with ALMA: CO, HDO and sulfur species," ASA Meeting, 2013.
- [28] NA, C., ESPOSITO, L., MCCLINTOCK, W., and BARTH, C., "Sulfur dioxide in the atmosphere of venus: Ii. modeling results," *Icarus*, vol. 112, no. 2, pp. 389 – 395, 1994.
- [29] PETTENGILL, G. H., FORD, P. G., and CHAPMAN, B. D., "Venus: Surface electromagnetic properties," *Journal of Geophysical Research: Solid Earth*, vol. 93, no. B12, pp. 14881–14892, 1988.
- [30] PETTENGILL, G. H., FORD, P. G., and WILT, R. J., "Venus surface radio-thermal emission as observed by magellan," *Journal of Geophysical Research: Planets*, vol. 97, no. E8, pp. 13091–13102, 1992.
- [31] PICKETT, H., POYNTER, R., COHEN, E., DELITSKY, M., PEARSON, J., and MULLER, H., "Submillimeter, millimeter, and microwave spectral line catalog," *Journal of Quantitative Spectroscopy and Radiative Transfer*, vol. 60, no. 5, pp. 883 – 890, 1998.
- [32] SAGAWA, H., "Terahertz remote sensing of the Venusian atmosphere: Observations Using the Nobeyama Millimeter Array," *Journal of the National Institute of Information and Communications Technology*, vol. 55, pp. 149–157, 2008.
- [33] SEIFF, A., KIRK, D. B., YOUNG, R. E., BLANCHARD, R. C., FINDLAY, J. T., KELLY, G. M., and SOMMER, S. C., "Measurements of thermal structure and thermal contrasts in the atmosphere of venus and related dynamical observations: Results from the four pioneer venus probes," *Journal of Geophysical Research: Space Physics*, vol. 85, no. A13, pp. 7903–7933, 1980.
- [34] STEFFES, P. G., KLEIN, M. J., and JENKINS, J. M., "Observations of the microwave emission of venus from 1.3 to 3.6 cm," *Icarus*, vol. 84, no. 1, pp. 83 – 92, 1990.
- [35] STEFFES, P. G., SHAHAN, P., BARISICH, G. C., and BELLOTTI, A., "Laboratory measurements of the 3.7-20 cm wavelength opacity of sulfur dioxide and carbon dioxide under simulated conditions for the deep atmosphere of venus," *Icarus*, 2014.
- [36] SULEIMAN, S. H., *Microwave Effects of Gaseous Sulfur Dioxide (SO₂) in the Atmospheres of Venus and Earth*. PhD thesis, Georgia Institute of Technology, May 1997.

- [37] SULEIMAN, S. H., KOLODNER, M. A., and STEFFES, P. G., “Laboratory measurement of the temperature dependence of gaseous sulfur dioxide (so₂) microwave absorption with application to the venus atmosphere,” *Journal of Geophysical Research: Planets*, vol. 101, no. E2, pp. 4623–4635, 1996.
- [38] ULICH, B., DAVIS, J. H., RHODES, P., and HOLLIS, J., “Absolute brightness temperature measurements at 3.5-mm wavelength,” *Antennas and Propagation, IEEE Transactions on*, vol. 28, pp. 367–377, May 1980.
- [39] VETUKHNOVKAYA, Y. N., *Radio astronomy measurements of Venus and several results from an interpretation of these measurements on the basis of AIS Venera-4 data*. PhD thesis, FIAN University, 1988.

THE MILLIMETER-WAVELENGTH SULFUR DIOXIDE ABSORPTION SPECTRA MEASURED UNDER SIMULATED VENUS CONDITIONS

Amadeo Bellotti

66 Pages

Directed by Professor Paul G. Steffes

The objective of the proposed research is to develop a mathematical model that accurately estimates the opacity of sulfur dioxide in a carbon dioxide atmosphere under conditions characteristic of the Venus troposphere based on extensive laboratory measurements. High precision measurements of the millimeter-wavelength properties of sulfur dioxide are being conducted under multiple pressure and temperatures. These measurements are being conducted in both W-band and F-band (2-3 and 3-4 millimeter-wavelengths). The results of this research will significantly improve the understanding of the millimeter-wavelength emission spectrum of Venus and possibly determine the source of variations in the Venus millimeter-wavelength emissions.